An inverse modelling study on the local volume changes during early growth of the fetal human brain

Z. Wang[*], B. Martin[†], J. Weickenmeier[‡] and K. Garikipati[§]

October 9, 2020

Abstract

We take a data-driven approach to deducing the local volume changes accompanying early development of the fetal human brain. Our approach uses fetal brain atlas MRI data for the geometric changes in representative cases. Using a nonlinear continuum mechanics model of morphoelastic growth, we invert the deformation field obtained from MRI registration to arrive at a field for the growth deformation gradient tensor. Our field inversion uses a combination of direct and adjoint methods for computing gradients of the objective function while constraining the optimization by the physics of morphoelastic growth. We thus infer a growth deformation gradient field that obeys the laws of morphoelastic growth. The errors between the MRI data and the forward displacement solution driven by the inverted growth deformation gradient field are found to be smaller than the reference displacement by well over an order of magnitude, and can be driven even lower. The results thus reproduce the three-dimensional growth during the early development of the fetal brain with controllable error.

1 Introduction

Like other organs, the fetal human brain undergoes large changes in volume and geometry during development *in utero*. A foundational understanding of these growth-induced changes can be gained from a *morphoelastic* treatment. Such an approach underlies the now accepted model of morphological development of most biological structures: Mass accretes, either due to cell growth and division, or from the deposition of extra-cellular matrix elements. Due to the elasticity of the newly grown (accreted) tissue, some energy is stored in it, and the relaxation of this energy occurs via an expansion of the tissue. The brain's grey and white matter are soft materials with molecular structures that are subjected to stress-dependent breakage of secondary bonds, and furthermore, are fluid-filled. There is, therefore, a rate-dependence to the mechanical response of the brain's constituent matter. However, on the time scales of days to weeks over which the brain undergoes morphological changes, viscous effects are fully relaxed, and elasticity prevails. Specifically, hyperelastic models governed by the equations of nonlinear elasticity describe the mechanical changes accompanying growth.

This is the foundation for the morphoelastic theory of growth, which relies upon a *growth deformation gradient tensor* as one component of a multiplicative decomposition of the total deformation gradient tensor. In general, it is incompatible, meaning that it cannot be expressed as the gradient of a smooth vector field. However, its product, conventionally written by pre-multiplication by the elastic deformation gradient tensor, is indeed compatible, since it expresses the total deformation gradient. The morphoelastic theory of growth has gained interest over the last two decades from the standpoint of neurodevelopmental studies that seek to explain the folding of the brain.

[*]Mechanical Engineering, University of Michigan

[†]Computer Science and Engineering, University of Michigan

[‡]Mechanical Engineering, Stevens Institute of Technology; Email: johannes.weickenmeier@stevens.edu

[§]Mechanical Engineering, Mathematics and Michigan Institute for Computational Discovery & Engineering, University of Michigan; corresponding author, Email: krishna@umich.edu

Folding, or sulcification and gyrification, of the brain is common in mammals including primates, cetaceans, pachyderms and ungulates. Folds form in the cortical layer of grey matter, and in species such as humans that demonstrate pronounced gyrencephaly, the sulci can be significantly deeper than the cortical thickness. A folded cortex confers a cognitive advantage by increasing the surface area enclosed within the skull, translating to greater capacity for intelligence. Normally developed human brains have a gyrification index (ratio of actual surface area to the surface area of an enveloping surface) approaching 2.55 [44]. Neurodevelopmental pathologies are associated with significant departures from this value. In humans, polymicrogyria (shallow, more frequent folding) is associated with developmental delays and epilepsy [23]. Pachygyria (shallow, less frequent and flatter folds) is associated with seizures, cognitive impairment and in rare cases, afflictions such as bipolar disorder [33]. Lissencephaly (abscence of folds) is associated with abnormal EEG patterns, intractable epilepsy [24] and cognitive impairment [28].

Fetal MRI data indicate that the human brain is almost perfectly smooth until 24 weeks of gestation [21, 15, 17], from which stage gyrification proceeds until well after birth. Therefore, there is a clear neurophysiological motivation to understand the physics governing cortical folding and the conditions for normal or pathological cortical folding. Incompatible morphoelastic growth in the cortical layer results in circumferential compression and causes an elastic buckling bifurcation. It is then followed by extreme strains leading to highly folded structures in the post-bifurcation regime. While a theory of axonal tension had been advanced to explain cortical folding under forces imposed by interconnected neurons [12], more recent studies of cutting followed by elastic relaxation on ferret brains established that axonal tension does not cause folding, while computational studies strongly suggested that incompatible growth does [41]. Bayly et al. [3] explained gyrification patterns by analytic and computational studies based on incompatible morphoelastic growth and Tallinen et al. [35] used experiments in a surrogate, polymeric gel model combined with nonlinear finite element computations to further support the morphoelastic theory of growth .[1]

Wrinkling of surfaces, such as seen on the cortex, and of interfaces, is a common phenomenon. In some cases it is influenced by mismatched elastic moduli between a thin elastic layer and an underlying substrate, a setting common to biological and non-biological thin films [43]. Among the former, it also may control the patterns of wrinkling of fruit and vegetable skins [42]. However, the essence of the phenomenon of brain folding does not depend on stiffness contrasts [31, 10, 11]; the Young's Modulus of cortical grey matter and of the white matter underlying it are of the same order of magnitude [7, 40]. Therefore, the elastic matter of the folding brain may be reasonably taken as homogeneous.

A number of recent studies have sought to explain aspects of brain folding by incompatible growth under linearized and, more appropriately, nonlinear morphoelasticity [3, 35, 4, 6, 7, 9, 19, 22, 34, 36]. While drawing upon insight from linearized buckling of beams, plates and shells [19, 22, 8], most of the computational work is based on finite strains in the post-bifurcation regime–albeit on analytic ellipsoidal shapes. This body of work has shed light on the mechanical conditions governing the development of the organ-wide pathologies of polymicrogyria, pachygyria and lissencephaly [6, 19, 9].

It is notable that the early-forming primary sulci and gyri in humans and other gyrencephalic species show a remarkable robustness of placement in normally developed brains [38]. This is emphasized in fetal brain atlases with data on the geometry of developing brains, such as those obtained from 67 individuals by Gholipour *et al.* [17]. After uniform scaling to normalize volumes, an "average" brain defined by computing the mean geometry showed well-resolved primary folds. This suggests that, when scaled for volume, the placement of those folds is consistent across individuals. Absent this persistence, the folds would have been smeared out in the averaged geometry. A second observation is that despite the organ scale lateral symmetry of the brain the sulci and gyri do not localize into symmetric modes of folding at all scales [21, 29] as seen in computational studies on high-symmetry reference shapes. These observations serve as motivations to identify the sequence of kinematic and mechanical steps that lead to precise placement of the primary folds as well as the range of variation in secondary and tertiary folds. Recent work studied the mechanisms of cell growth and migration and linked them to the developing pattern of the early folds [36, 32].

Here, we take a broader view, seeking to deduce the local volume changes that develop throughout

[1] Albeit, solved as elastic unloading from the folded configuration with first-order dynamics added to numerically stabilize the system against bifurcations.

the brain and drive its expansion as well as folding by incompatible, morphoelastic growth. Our approach is a data-driven one. Using magnetic resonance imaging (MRI) data on the geometric changes of the fetal brain, recorded weekly, we seek to solve a series of inverse problems to arrive at the spatially varying growth deformation gradient tensor of the morphoelastic theory. The methods we use begin with MRI segmentation and computational mesh generation to enable image registration across successive weeks of brain development. These steps, themselves involving inverse modelling, provide us with the geometric data for the final stage of physics-constrained inference. Here, we combine direct and adjoint methods for computing gradients of objective functions in a generalized optimization setting, subject to the constraint imposed by the physics of morphoelastic growth. This will leave us with mechanics-constrained geometric data in the form of the precisely defined growth deformation tensor that describes the three-dimensional development of the fetal brain. From this basis, further physically well-founded inference will be possible on the dynamics of fetal brain development.

The morphoelastic growth model is discussed in §2, the inverse problem for the growth deformation tensor and tests with synthetic data appear in §3. MRI segmentation of fetal brain atlas data and computational mesh generation with it appear in §4. The MRI registration problem is discussed in §5, and the extraction of morphoelastic growth deformation data in §6. Results for the inferred growth deformation gradient tensor are in §7, and conclusions in §8

2 The theory of morphoelastic growth

The theory of morphoelastic growth is well-established and traces its roots to multiplicative plasticity, and even before that to multiplicative theormoelasticity. For a discussion of the kinematics we direct the reader to Ref. [13], to Refs [14, 27] for its coupling with mass transport, and to Ref. [2] for a perspective of growth and remodelling. A complete treatment that includes the mathematical background and a proper placement of the theory within nonlinear elasticity can be found in Ref. [18]. The treatment that follows here is rigorous, but eschews formalism in favor of accessibility of the important ideas.

Given the displacement field $\boldsymbol{u} \in \mathbb{R}^3$, and the reference position of material points $\boldsymbol{X} \in \mathbb{R}^3$, the deformation gradient tensor is $\boldsymbol{F} = \mathbf{1} + \partial \boldsymbol{u}/\partial \boldsymbol{X}$, where $\mathbf{1}$ is the isotropic tensor. The multiplicative decomposition of $\boldsymbol{F}$ that underlies the theory splits it into elastic and growth components, $\boldsymbol{F}^{\mathrm{e}}$ and $\boldsymbol{F}^{\mathrm{g}}$, respectively, so that $\boldsymbol{F} = \boldsymbol{F}^{\mathrm{e}}\boldsymbol{F}^{\mathrm{g}}$.

Incompatibility is admitted by this decomposition in that $\boldsymbol{F}^{\mathrm{g}}$, which we think of as driving morphoelastic growth, is not, in general, obtained as a gradient field in the manner that $\boldsymbol{F}$ arises from $\boldsymbol{u}$. It therefore does not satisfy the classical kinematic compatibility conditions that $\boldsymbol{F}$ does.

As explained in the Introduction, we work within the theory of hyperelasticity. We adopt a neo-Hookean strain energy density function ψ from [36], which depends exclusively on the elastic right Cauchy-Green tensor $\boldsymbol{C}^{\mathrm{e}} = \boldsymbol{F}^{\mathrm{e}^{\mathrm{T}}}\boldsymbol{F}^{\mathrm{e}}$,

$$\psi(\boldsymbol{C}^e) = \frac{1}{4}\lambda\left(\det\boldsymbol{C}^{\mathrm{e}} - 1\right) - \frac{1}{2}\left(\frac{1}{2}\lambda + \mu\right)\log\det\boldsymbol{C}^{\mathrm{e}} + \frac{1}{2}\mu(\mathrm{tr}\boldsymbol{C}^{\mathrm{e}} - 3), \tag{1}$$

where μ and λ are the standard Lamé parameters. The first Piola-Kirchhoff stress tensor $\boldsymbol{P}$ follows as the derivative of the strain energy W:

$$\boldsymbol{P} = \frac{\partial\psi}{\partial\boldsymbol{F}^e} = \mu\boldsymbol{F}^e + \frac{1}{2}\lambda J^c\boldsymbol{F}^{e-T} - \left(\frac{1}{2}\lambda + \mu\right)\boldsymbol{F}^{e-T}, \tag{2}$$

where $J^{\mathrm{c}} = \det\boldsymbol{F}^e$. The first Piola-Kirchhoff stress is governed by the quasistatic balance of linear momentum with no body force:

$$\nabla\cdot\boldsymbol{P} = \mathbf{0} \text{ in } \Omega, \quad \boldsymbol{u} = \bar{\boldsymbol{u}} \text{ on } \partial\Omega_u, \quad \boldsymbol{P}\boldsymbol{N} = \bar{\boldsymbol{t}} \text{ on } \partial\Omega_P, \tag{3}$$

where $\Omega \subset \mathbb{R}^3$ denotes the domain, which is the brain, and its Dirichlet and Neumann boundaries are Ω_u and Ω_P, satisfying $\overline{\Omega_u \cup \Omega_P} = \partial\Omega$ and $\Omega_u \cap \Omega_P = \emptyset$. In this study, $\bar{t} = \mathbf{0}$ and deformation will be driven by $\boldsymbol{F}^{\mathrm{g}}$ resulting from observed displacement data.

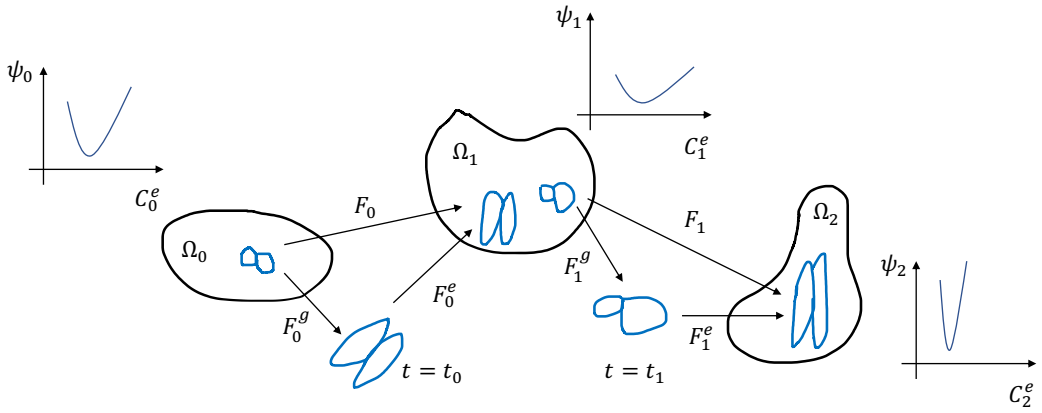

Figure 1: Classical morphoelastic growth presumes that the entire path of growth and morphogenesis can be described kinematically with the initial state of the brain as the reference configuration. In the case of fetal brain development and the emergence of new material, we posit that this assumption proves problematic and propose a theory of evolving reference configurations. Specifically, we split the growth path into multiple individual steps defined by their own reference configuration Ω_τ, kinematics and strain energy density functions defined on them.

2.1 A theory of evolving reference configurations

The theory of morphoelastic growth has traditionally been applied to a fixed reference configuration, relative to which the tensors $\boldsymbol{F}$ and $\boldsymbol{F}^{\mathrm{g}}$ have been defined. For finite growth and morphogenesis, which characterise fetal brain development, however, this theory proves inadequate. Its premise is that the entire path of growth and morphogenesis can be described kinematically with the initial state of the brain as the reference configuration. This assumption proves problematic when taken to the logical conclusion that the reference configuration is therefore the singularity when the first brain cell appears. Furthermore, it does not account for mass appearing at some time, say τ, introducing material points where none existed before, thus defining the reference state from which the newly formed material deforms. Finally, it does not address the evolution of local material properties, in this case represented by the strain energy density function on the reference configuration, which can change as growth and morphogenesis proceed. To circumvent these difficulties, we define a continuously evolving reference configuration, Ω_τ, which coincides with the deformed configuration resulting from all morphoelastic processes from times $t \leq \tau$ (see Figure 1).

In this setting, the kinematics of finite strain multiplicative morphoelasticity is elaborated upon by time parameterization yielding $\boldsymbol{F}_\tau, \boldsymbol{F}^{\mathrm{g}}_\tau, \boldsymbol{F}^{\mathrm{e}}_\tau$, that satisfy:

$$\boldsymbol{F}_\tau = \mathbf{1} + \frac{\partial \boldsymbol{u}_\tau}{\partial \boldsymbol{X}_\tau}, \tag{4}$$

$$\boldsymbol{F}_\tau = \boldsymbol{F}^{\mathrm{e}}_\tau \boldsymbol{F}^{\mathrm{g}}_\tau, \tag{5}$$

$$\boldsymbol{C}^{\mathrm{e}}_\tau = \boldsymbol{F}^{\mathrm{e}}_\tau \boldsymbol{F}^{\mathrm{e}^{\mathrm{T}}}_\tau, \tag{6}$$

and the strain energy density function is similarly written as

$$\psi_\tau(\boldsymbol{C}^{\mathrm{e}}_\tau) = \frac{1}{4}\lambda\left(\det \boldsymbol{C}^{\mathrm{e}}_\tau - 1\right) - \frac{1}{2}\left(\frac{1}{2}\lambda + \mu\right)\log\det \boldsymbol{C}^{\mathrm{e}}_\tau + \frac{1}{2}\mu(\mathrm{tr}\boldsymbol{C}^{\mathrm{e}}_\tau - 3). \tag{7}$$

Finally, the stress and governing partial differential equation are:

$$\boldsymbol{P}_\tau = \frac{\partial \psi_\tau}{\partial \boldsymbol{F}^{\mathrm{e}}_\tau} = \mu \boldsymbol{F}^{\mathrm{e}}_\tau + \frac{1}{2}\lambda J^c \boldsymbol{F}^{\mathrm{e}^{-\mathrm{T}}}_\tau - \left(\frac{1}{2}\lambda + \mu\right)\boldsymbol{F}^{\mathrm{e}^{-\mathrm{T}}}_\tau, \tag{8}$$

$$\nabla_\tau \cdot \boldsymbol{P}_\tau = \mathbf{0} \text{ in } \Omega_\tau, \quad \boldsymbol{u}_\tau = \bar{\boldsymbol{u}}_\tau \text{ on } \partial\Omega_{\tau_u}, \quad \boldsymbol{P}_\tau \boldsymbol{N}_\tau = \bar{\boldsymbol{t}}_\tau \text{ on } \partial\Omega_{\tau_P}. \tag{9}$$

The strain energy density, ψ_τ, while written here in time-independent functional form, could also evolve in general. This reflects the understanding that the strain energy density, like the free energy, is defined relative to some reference. Here, as Figure 1 suggests, it is redefined at each reference state, Ω_τ. In practice, a discrete time parameterization is adopted at instants $\tau \in \{t_0, t_1, \dots\}$. This is natural for data acquisition and computations.

3 An inverse problem posed on the geometry of the developing brain

In §4–6 we describe the steps by which we arrive at geometric field data, $\widehat{\boldsymbol{u}}$ that represents displacements during growth of the developing brain. With these data, we seek to solve an inverse problem for the growth tensor field $\boldsymbol{F}^{\mathrm{g}}_\tau$ and displacement field $\boldsymbol{u}_\tau$ such that the error $\widehat{\boldsymbol{u}}_\tau - \boldsymbol{u}_\tau$ is minimized under the constraint of the physics expressed in Equations (4–9). The data field $\widehat{\boldsymbol{u}}_\tau$ will be interpolated from pointwise displacement vectors $\widehat{\boldsymbol{d}}_{\tau_1}, \dots \widehat{\boldsymbol{d}}_{\tau_N}$ at N points $\boldsymbol{X}_{\tau_1}, \dots \boldsymbol{X}_{\tau_N}$. Similarly, we will use the finite-dimensional version $\boldsymbol{F}^{\mathrm{g}^h}_\tau$ of the unknown growth tensor and the corresponding displacement field, $\boldsymbol{u}^h_\tau$. Our approach is to use the finite-dimensional weak form of the governing equations (9), which is expressed as follows in terms of $\boldsymbol{u}^h_\tau$ and $\boldsymbol{F}^{\mathrm{g}^h}_\tau$:

For some $\boldsymbol{u}^h_\tau \in \mathscr{S}^h \subset \mathscr{S}$, where $\mathscr{S}^h = \{\boldsymbol{u}^h_\tau \in \mathscr{H}^1(\Omega) \mid \boldsymbol{u}^h_\tau = \overline{\boldsymbol{u}}_\tau \text{ on } \partial\Omega_u\}$, and $\forall\ \boldsymbol{w}^h \in \mathscr{V}^h \subset \mathscr{V}$, where $\mathscr{V}^h = \{\boldsymbol{w}^h \in \mathscr{H}^1(\Omega) \mid \boldsymbol{w}^h = 0 \text{ on } \partial\Omega_u\}$, the finite-dimensional (Galerkin) weak form of the problem is satisfied:

$$\int_\Omega \nabla \boldsymbol{w}^h : \boldsymbol{P}_\tau(\boldsymbol{u}^h_\tau, \boldsymbol{F}^{\mathrm{g}^h}_\tau)\mathrm{d}V - \int_{\partial\Omega_P} \boldsymbol{w}^h \cdot \boldsymbol{t}\mathrm{d}S = 0. \tag{10}$$

In a forward solution of the weak form, a constitutive model would be written for $\boldsymbol{F}^{\mathrm{g}^h}_\tau$. This approach, with some variations, has been followed almost universally in the literature up to this point [3, 35, 4, 6, 7, 9, 19, 22, 34, 36]. The determination of $\boldsymbol{F}^{\mathrm{g}^h}_\tau$ by solution of an inverse problem is a significant departure in the current work. By seeking to invert a tensor field it also stands in contrast to classical inverse problems in mathematical physics that infer a small number of scalar parameters. We decompose Ω into element sub-domains Ω_{e}, for $e = 1, \dots n_{\mathrm{el}}$. The variations $\boldsymbol{w}^h$, trial displacement solutions $\boldsymbol{u}^h$ and growth tensor $\boldsymbol{F}^{\mathrm{g}^h}_\tau$ are defined by using a finite number of basis functions in each element,

$$\boldsymbol{w}^h_e = \sum_{a=1}^{n} \boldsymbol{c}_a N_a, \qquad \boldsymbol{u}^h_{\tau_e} = \sum_{a=1}^{n} \boldsymbol{d}_{\tau_a} N_a, \qquad \boldsymbol{F}^{\mathrm{g}^h}_{\tau_e} = \sum_{a=1}^{m} \boldsymbol{\chi}_{\tau_a} M_a \tag{11}$$

where $\boldsymbol{c}_a, \boldsymbol{d}_{\tau_a} \in \mathbb{R}^3$, $\boldsymbol{\chi}_{\tau_a} \in \mathbb{R}^{3\times 3}$, n is the dimensionality of the function spaces $\mathscr{S}^h$ and $\mathscr{V}^h$, m is the dimensionality of the expansion for $\boldsymbol{F}^{\mathrm{g}^h}_\tau$ and N_a, M_a represent basis functions. If the growth tensor is assumed to be diagonal and anisotropic, the dimensionality could be reduced to n, and the diagonal terms are defined by:

$$\mathrm{diag}\left(\boldsymbol{F}^{\mathrm{g}^h}_{\tau_e}\right) = \sum_{a=1}^{n} \widetilde{\boldsymbol{\chi}}_{\tau_a} M_a \tag{12}$$

where $\widetilde{\boldsymbol{\chi}}_{\tau_a} \in \mathbb{R}^3$. This form was motivated by the total deformation gradient tensor, which when extracted from MRI data on normative, developing fetal brains in Gholipour *et al.*'s atlas [17] by the methods in §4–6, was found to be similarly diagonally dominant and anisotropic. We made this assumption throughout the following of this communication, and dispensed with the tildes on $\boldsymbol{\chi}_a$.

We define the residual vector arising from finite element assembly of the weak form:

$$\boldsymbol{R}_\tau(\boldsymbol{d}_\tau, \boldsymbol{\chi}_\tau) = \mathop{\mathcal{A}}_{e} \left(\int_{\Omega_e} \sum_{a=1}^{n} \nabla N_a \cdot \boldsymbol{P}(\boldsymbol{u}^h_\tau(\boldsymbol{d}_\tau), \boldsymbol{F}^{\mathrm{g}^h}_\tau(\boldsymbol{\chi}_\tau))\mathrm{d}V - \int_{\partial\Omega_{\mathrm{P_e}}} N_a \boldsymbol{t}\mathrm{d}S \right) \tag{13}$$

where $\mathop{\mathcal{A}}_{e}$ denotes the assembly operator over the elements, and the arbitrariness of the degrees of freedom corresponding to the variations has been used, as is the practice in the variational setting.

Recall that the dimensionality of the vector $\boldsymbol{R}_\tau$ is the total number of unknown displacement degrees of freedom. The discretized, Galerkin weak form of the problem is then $\boldsymbol{R}_\tau(\boldsymbol{d}_\tau, \boldsymbol{\chi}_\tau) = \boldsymbol{0}$. In the current setting, it represents the physics that constrains the inverse problem, for whose solution we adopt two approaches.

3.1 Inverse solution for $\boldsymbol{F}_\tau^{\mathrm{g}}$ by gradient descent on a loss function

In this approach we directly define the field data $\widehat{\boldsymbol{u}}$ as a finite-dimensional function:

$$\widehat{\boldsymbol{u}}_{\tau_e} = \sum_{a=1}^{n} \widehat{\boldsymbol{d}}_{\tau_a} N_a \tag{14}$$

and use it instead of $\boldsymbol{u}_\tau^h$ in the weak form (10) and residual equation (13) to arrive at $\boldsymbol{R}_\tau(\widehat{\boldsymbol{d}_\tau}, \boldsymbol{\chi}_\tau)$. The loss function is

$$\ell_{\mathrm{gd}}(\boldsymbol{R}_\tau) = |\boldsymbol{R}_\tau| \tag{15}$$

defined via the Euclidean norm. We use gradient descent algorithms, and their variants, to find

$$\boldsymbol{\chi}_\tau = \arg\min_{\widetilde{\boldsymbol{\chi}}} \ell_{\mathrm{gd}}(\boldsymbol{R}_\tau(\widehat{\boldsymbol{d}_\tau}, \widetilde{\boldsymbol{\chi}})). \tag{16}$$

Note that the form of the loss, $\ell_{\mathrm{gd}} = |\boldsymbol{R}_\tau|$, means that the exact satisfaction of the constraint $\boldsymbol{R}(\widehat{\boldsymbol{d}}, \boldsymbol{\chi}) = \boldsymbol{0}$ is the optimal solution to (16). As in many high-dimensional, nonlinear optimization problems, this solution is not attainable, in general. Instead, we seek to arrive at $\ell_{\mathrm{gd}} < \varepsilon$ for some tolerance ε using either the classical gradient descent algorithm or one of its variants. The field $\boldsymbol{F}_\tau^{\mathrm{g}^h}$ is then recovered by Equation (12).

3.2 Solution of the inverse problem by adjoint-based gradient optimization

With $\widehat{\boldsymbol{u}}_\tau$ written as in Equation (14) we solve the following minimization problem, beginning with the loss redefined as the L^2-norm of the error

$$\begin{aligned} \ell_{L^2} &= \|\widehat{\boldsymbol{u}}_\tau(\widehat{\boldsymbol{d}}_\tau) - \boldsymbol{u}_\tau^h(\boldsymbol{d}_\tau(\widetilde{\boldsymbol{\chi}}_\tau))\|_2, \\ \boldsymbol{\chi}_\tau &= \arg\min_{\widetilde{\boldsymbol{\chi}}_\tau} \ell_{L^2}, \quad \text{such that } \boldsymbol{R}_\tau(\boldsymbol{d}_\tau, \boldsymbol{\chi}_\tau) = \boldsymbol{0}. \end{aligned} \tag{17}$$

The minimization is solved classically, by computing gradients of the loss ℓ_{L^2}. Importantly, the PDE constraint $\boldsymbol{R}_\tau(\boldsymbol{d}_\tau, \boldsymbol{\chi}_\tau) = \boldsymbol{0}$ makes $\boldsymbol{d}_\tau$ an implicit function of $\boldsymbol{\chi}$. This makes the functional derivatives $\delta\ell_{L^2}/\delta\boldsymbol{d}_\tau$ challenging to compute. The obvious approach is to solve the PDE constraint repeatedly for a range of values of $\boldsymbol{\chi}_\tau$ and construct the implicit derivative by numerical differentiation. In addition to the expense of a large number of PDE forward solves for a single derivative evaluation, numerical differentiation is noisy and ultimately introduces instabilities. The well-established alternative is to employ the adjoint of the Jacobian of the PDE constraint with respect to $\boldsymbol{d}_\tau$ to compute $\delta\ell_{L^2}/\delta\boldsymbol{d}_\tau$. The Jacobian arises in the complete first-order Taylor expansion of the PDE constraint equation, and allows the computation of $\delta\ell_{L^2}/\delta\boldsymbol{d}_\tau$ with a single adjoint solution per step. We have adopted this approach to PDE constrained optimization here, and refer to it as *adjoint-based gradient optimization*. In this work we use the *L-BFGS-B* optimization algorithm from *SciPy* [37] with the aid of the *dolfin-adjoint* [26] package for adjoint-based gradient optimization.

3.3 Algorithm testing with synthetic data

The gradient descent and adjoint-based gradient optimization approaches were first tested against synthetic data for nonuniform but continuous growth tensor fields. These fields were obtained by solving a three-dimensional, steady state diffusion problem for a scalar field c and defining $\boldsymbol{F}^{\mathrm{g}}$ to be a function of this argument. The steady state diffusion problem is:

$$\nabla^2 c = 0 \quad \text{in} \quad \Omega, \tag{18}$$

$$c = 1 \quad \text{on} \quad \Gamma_{\mathrm{v}}, \tag{19}$$

$$c = 1.2 \quad \text{on} \quad \Gamma_{\mathrm{c}}, \tag{20}$$

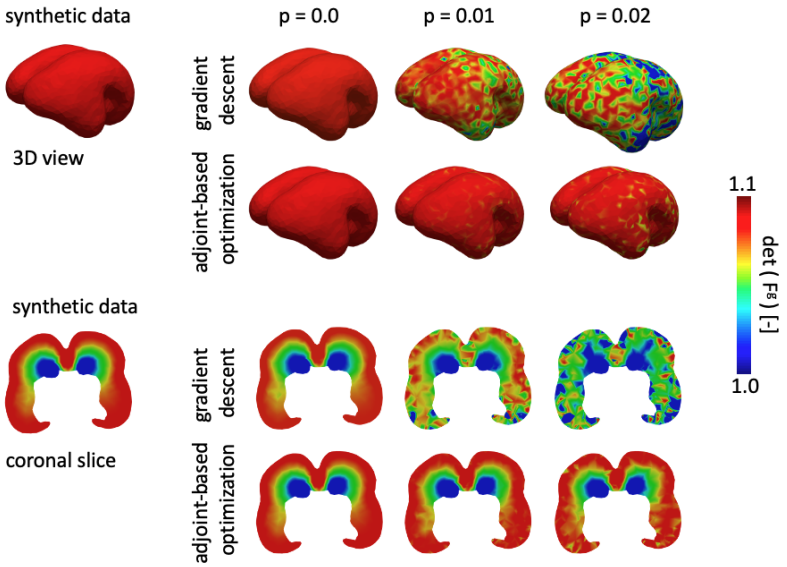

Figure 2: We generated synthetic displacement fields on the fetal brain mesh of week 24 in order to test the accuracy of our two optimization algorithms. We show the solution of the inverse problem in the form of the inferred $\det \boldsymbol{F}^g$ fields using the gradient descent and the adjoint-based optimization approach. Top rows show the three dimensional view and the bottom rows shows the coronal view for three levels of superposed noise p.

where Ω was taken as the normative fetal brain geometry at week 21 from the atlas of Gholipour *et al.* [17], Γ_{v} is the interface between the ventricles and sub-cortex and Γ_{c} is the outer surface of the cortex. The growth deformation gradient tensor is chosen to be diagonal, but anisotropic, and of the form:

$$\widehat{\boldsymbol{F}}^{\mathrm{g}} = \mathbf{1} + 0.15(c-1)\boldsymbol{e}_1 \otimes \boldsymbol{e}_1 + 0.05(c-1)\boldsymbol{e}_2 \otimes \boldsymbol{e}_2 + 0.1(c-1)\boldsymbol{e}_3 \otimes \boldsymbol{e}_3. \tag{21}$$

The field of determinant of the synthetic $\widehat{\boldsymbol{F}}^{\mathrm{g}}$ is shown in Figure 2. The forward problem of morphoelastic growth, described in Equations (4–13) was then solved by the finite element method for time $\tau = 0$ on a mesh with 27306 tetrahedral elements using the `FEniCS` open source code [1]. The neo-Hookean strain energy density function (1) was used in the the nearly incompressible limit with $\lambda = 82214.8$ Pa and $\mu = 16777.8$ Pa [36], corresponding to a Poisson ratio $\nu = 0.49$ in the infinitesimal strain regime. We denote the resulting synthetic displacement field by $\boldsymbol{u}_{\mathrm{s}}$. To model the noise present in the displacement fields extracted from the fetal brain atlas, varying amounts of Gaussian noise were applied to the synthetic data. For displacement fields with applied noise fraction p, nodal displacements were offset by $\delta\boldsymbol{u} \sim \mathcal{N}(0, p\boldsymbol{u}_c)$, where $p \in \{0, 0.01, 0.02\}$.

3.3.1 Inverse solution by gradient descent on synthetic data

The problem as posed in §3.1 and 3.2 admits a multitude of feasible solutions, and optimal solutions, if they are obtained also could be non-unique. This situation is typical of inverse problems. The optimization algorithms navigate a high-dimensional landscape of feasible solutions seeking the optimal one. Furthermore, there is the stiffness induced by the nonlinearity of the PDE constraint in the form of the residual (13). This combination can lead to slow convergence or even divergence. Aiming to mollify this problem, we linearly subdivide the synthetic data $\boldsymbol{u}_{\mathrm{s}}$ into some number of, in this case ten, steps. The gradient descent approach at step i uses $\widehat{\boldsymbol{u}}_i = \frac{i}{10}\boldsymbol{u}_c$. The initial guess for the nodal values of $\boldsymbol{F}^{\mathrm{g}}$ at step $i \neq 0$, i.e., the nodal tensor unknowns $\boldsymbol{\chi}_i$, was the inferred $\boldsymbol{F}^g$ from the previous step such that $\boldsymbol{\chi}_{i_0} = \boldsymbol{\chi}_{i-1_{\mathrm{final}}}$. The initial guess for $\boldsymbol{\chi}$ at Step 1 was chosen to be the diagonalized deformation gradient tensor constructed by $\frac{1}{10}\boldsymbol{u}_c$, i.e. the target displacement at Step 1. Specifically, we project diagonal components of the deformation gradient tensor to the nodes by solving an L^2

Noise, p	$\|\widehat{\boldsymbol{u}}\|_\infty$	$\|\boldsymbol{F}^g\|_\infty$	$\|e(\boldsymbol{u})\|_2^{\mathrm{gd}}$	$\|e(\boldsymbol{F}^g)\|_2^{\mathrm{gd}}$	$\|e(\boldsymbol{u})\|_2^{\mathrm{adj}}$	$\|e(\boldsymbol{F}^g)\|_2^{\mathrm{adj}}$
0.00	5.212×10^{-1}	1.767	6.697×10^{-4}	1.640×10^{-3}	6.415×10^{-5}	5.148×10^{-3}
0.01	5.196×10^{-1}	1.767	9.978×10^{-3}	7.352×10^{-2}	5.476×10^{-4}	1.053×10^{-2}
0.02	5.284×10^{-1}	1.767	1.753×10^{-2}	1.183×10^{-1}	1.104×10^{-3}	2.001×10^{-2}

Table 1: Results of the inverse problem for synthetic data. The superscripts "gd" and "adj" denote the solution obtained via using gradient descent with the Adam optimizer and adjoint-based optimization, respectively.

projection problem:

$$\int_\Omega \boldsymbol{w}_{1_0} : \left(\boldsymbol{\chi}_{1_0} - \mathrm{diag}\,(\boldsymbol{F})\right) \mathrm{d}V = 0, \tag{22}$$

with $\boldsymbol{w}_{1_0}$ being the variations on $\boldsymbol{\chi}_{1_0}$. We define the volume averaged L^2 error for the final inferred $\boldsymbol{F}^g$ at the tenth step as:

$$\|e(\boldsymbol{F}^g)\|_2 := \left(\frac{1}{V} \int_\Omega |\boldsymbol{F}^g_{10} - \widehat{\boldsymbol{F}}^g|^2_{\mathrm{F}} \mathrm{d}V \right)^{1/2}, \tag{23}$$

where $|\bullet|_{\mathrm{F}}$ denotes the Frobenius norm and $\widehat{\boldsymbol{F}}^{\mathrm{g}}$ is the field from Equation (21). With the inferred $\boldsymbol{F}^g_{10}$, we then evaluate the displacement by solving the forward elasticity problem, and evaluate the volume averaged L^2-error by

$$\|e(\boldsymbol{u})\|_2 := \left(\frac{1}{V} \int_\Omega |\boldsymbol{u} - \widehat{\boldsymbol{u}}|^2 \mathrm{d}V \right)^{1/2}. \tag{24}$$

Gradient descent updates were driven by the Adam optimizer with default parameters [25]. For steps 1-9, 10,000 epochs were used with learning rate decay given by $\eta_t = \frac{\eta_{t-1}}{1+(5\times10^{-8})t}$ and $\eta_0 = 10^{-4}$. To ensure convergence on the final step, 100,000 epochs were used with learning rate decay given by $\eta_t = \frac{\eta_{t-1}}{1+(2\times10^{-9})t}$ and $\eta_0 = 10^{-3}$.

Figure 2 shows $\det \widehat{\boldsymbol{F}}^{\mathrm{g}}$ inferred by gradient descent from synthetic data at different level of noise. Also shown in Table 1, gradient descent with the Adam optimizer allows inference of an $\boldsymbol{F}^{\mathrm{g}}$ field with volume-averaged L^2-error that is three orders of magnitude lower (fifth column) than the L^∞-norm of the applied $\boldsymbol{F}^{\mathrm{g}}$ for synthetic data generation, and even with noise fraction $p = 0.02$ remains an order of magnitude lower. However, the inferred $\boldsymbol{F}^{\mathrm{g}}$ field appears less smooth when obtained from the noisy data. We also have included the volume-averaged L^2-error in the forward displacement (fourth column) computed by applying the gradient descent-inferred $\boldsymbol{F}^{\mathrm{g}}$ field. For synthetic data without noise, the volume-averaged L^2-error is three orders of magnitude lower than the L^∞-norm of $\widehat{\boldsymbol{u}}$ and one order of magnitude lower for noise with $p = 0.02$.

3.3.2 Inverse solution by adjoint-based gradient optimization

As discussed in §3.2 adjoint-based gradient optimization involves the forward solution of the PDE constraint $\boldsymbol{R}(\boldsymbol{d}, \boldsymbol{\chi}) = \boldsymbol{0}$ at each step of the algorithm–see Equation (17). As also expressed there, this forward solution is driven by the inferred nodal growth tensor field $\boldsymbol{\chi}$ at each iteration. This forward problem is numerically stiff due to the nonlinearity, near-incompressibility and complex geometry of the brain. While the adjoint solution step to determine gradients typically poses no difficulty, divergence of the forward solution will cause the termination of the overall algorithm. Therefore, we now linearly subdivide the inferred $\boldsymbol{\chi}$ into 100 steps in driving the forward solution. The initial guess for $\boldsymbol{\chi}$ was again chosen to be the diagonalized deformation gradient tensor constructed from $\boldsymbol{u}_{\mathrm{s}}$.

Figure 2 and Table 1 also includes the results obtained by adjoint-based gradient optimization. Using noise-free data, the volume-averaged L^2-error in the inferred $\boldsymbol{F}^g$ is higher than that obtained by the gradient descent approach, but the volume-averaged L^2-error in the forward displacement solution

obtained as an inherent part of the adjoint-based gradient optimization approach is about one order of magnitude smaller than the corresponding error obtained by gradient descent. The superiority of the adjoint-based approach is more apparent in the presence of noise, improving to an order of magnitude lower volume-averaged L^2-error for $\boldsymbol{u}$ and $\boldsymbol{F}^{\mathrm{g}}$ over the gradient descent approach for $p = 0.02$. Additionally, the inferred $\boldsymbol{F}^{\mathrm{g}}$ field is smoother than that obtained by gradient descent. The adjoint-based approach is, in general, more computationally expensive since it needs one evaluation of the adjoint solution per step. Nevertheless, given these performance metrics, we choose to exclusively use the adjoint-based gradient optimization approach with the real MRI data from the fetal brain atlas, because of the inevitability of noise therein.

4 MRI Segmentation and FE Model Generation

We obtained data on brain geometries from a spatiotemporal magnetic resonance imaging (MRI) atlas of the fetal brain developed for the study of early brain growth [16]. Based on MRIs of 81 normal fetuses scanned between gestational weeks 19 and 39, Gholipour *et al.* created a four-dimensional atlas of brain development during the second half of gestation and covering weeks 21 through 37 [17]. Six to eight scans were used for the reconstruction of each week's atlas. The automatic atlas generation includes repeated motion correction, super-resolution volume reconstruction, brain mask segmentation, rigid alignment to the atlas space and intensity homogenization [16]. The resulting atlas clearly illustrates the temporally and spatially heterogeneous growth during early *in utero* brain development, including numerous instances of folding and creasing. In a first step, the present work focuses on weeks 21 through 25 during which the first major elastic bifurcation occurs, and from which the central sulcus (CS) emerges [20]. For each gestational week, we created a finite element model of the brain from the respective MR images using the `ScanIP` software environment of Simpleware (Synopsys, Mountain View CA), see Figure 3. In a semi-automatic segmentation procedure, we delineated the cortex, subcortex and lateral ventricles based on grayscale contrast and created a three-dimensional reconstruction of these structures [39]. The software converted these segmentations into a volumetric model consisting of tetrahedral elements. We prescribed a minimum and maximum element edge length of 2.0mm and 2.5mm, respectively, and obtained meshes with a total number of 68849 elements for the model of week 21, 78385 elements for week 22, 83000 elements for week 23, 97138 elements for week 24 and 172289 elements for week 25. The number of elements and nodes of each subregion are summarized in Table 2. Based on our segmentations, we observe that the total brain volume, i.e. cortex and subcortex, increases by 130% and ventricular volume increases by 17% between weeks 21 and 25. Specifically, cortical volume changes from 17155 mm^3 at week 21, to 20651 mm^3 at week 22, 20468 mm^3 at week 23, 26099 mm^3 at week 24 and 35232 mm^3 at week 25; subcortical volume increases from 23834 mm^3 at week 21, to 29159 mm^3 at week 22, 33056 mm^3 at week 23, 41360 mm^3 at week 24 and 58646 mm^3 at week 25; and ventricular volume changes from 5079 mm^3 at week 21, to 5176 mm^3 at week 22, 4011 mm^3 at week 23, 4527 mm^3 at week 24 and 5946 mm^3 at week 25. The rostral-caudal brain length increases by 29.5% between weeks 21 (59.86 mm) and 25 (77.54 mm); the width of the brain increases by 26.4% between weeks 21 (49.31 mm) and 25 (62.33 mm); and the height of the brain increases by 33.8% between weeks 21 (39.19 mm) and 25 (52.44 mm).

5 MRI Registration Framework

The continuous morphological changes of the fetal brain during *in utero* development are inherently contained in the fetal brain atlas described previously. To determine the incremental brain deformations driven by growth between consecutive gestational weeks, we use a previously developed registration method that determines the non-rigid spatial transformation between two MR images that maximizes the congruence of image intensities. Specifically, we built on the work of Pawar et al. [30] who optimized their algorithm for large deformations and topological changes between medical images. The source image $I_1(f(\boldsymbol{x}, t))$ and the target image $I_2(\boldsymbol{x})$ are both embedded in hierarchical

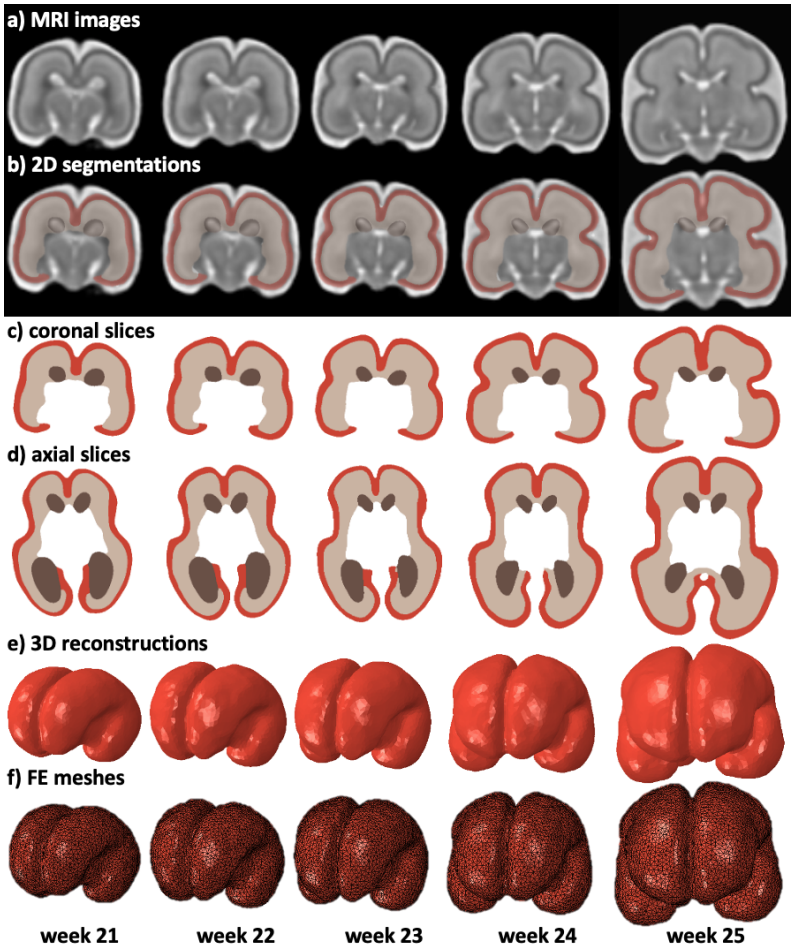

Figure 3: MR image segmentation and finite element model generation. We use a) structural MRIs from gestational weeks 21 through 25 and create 3D reconstructions based on a semi-automatic segmentation process. b) We delineate the cortex, subcortex and ventricles based on their grayscale thresholding and manual correction. c-d) show coronal and axial slices of the segmentation, respectively. The fully e) three-dimensional reconstructions are converted into f) volumetric finite element models that consist of tetrahedral elements.

model	week 21		week 22		week 23		week 24		week 25	
	#e	#n	#e	#n	#e	#n	#e	#n	#e	#n
cortex	25747	8262	29363	9439	29873	9623	34618	11188	97945	14957
subcortex	35749	8712	41996	9995	46852	10894	55066	12911	65217	15576
ventricles	7353	2106	7026	2068	6275	1881	7454	2157	9127	2638
total	68849	14262	78385	16204	83000	17095	97138	19982	172289	25197

Table 2: Mesh properties of our five finite element models for gestational weeks 21 through 25. Proportional to the increase in mesh size, total brain volume increases by 130% during this time period. #e = number of elements; #n = number of nodes.

truncated B-spline objects with the spatial transformation function $f(\boldsymbol{x}, t)$ given by [30]

$$f(\boldsymbol{x}, t) = \sum_{m=1}^{N_b} \boldsymbol{P}_m(t)\phi_m(\boldsymbol{x}), \tag{25}$$

where $\mathbf{P}_m(t)$ are the control points associated with the trivariate basis functions $\phi_m(\boldsymbol{x})$, and N_b represents the total number of basis functions. As part of the registration process, the transformation

function $f(\boldsymbol{x},t)$ is incrementally varied until dissimilarities between source and target image are minimal. To that end, we followed the proposed energy functional $E(f(\boldsymbol{x},t))$ proposed by Pawar et al. which accounts for intensity differences and penalizes non-smoothness of the deformation field [30]. The minimization of the energy functional is achieved by posing it as an L^2 gradient flow, thus simplifying the optimization problem to a partial differential equation. The energy functional takes the following form [30]

$$\begin{aligned} E(f(\boldsymbol{x},t)) = &\int_\Omega g(\boldsymbol{x},t)\left(I_2(\boldsymbol{x}) - I_1(f(\boldsymbol{x},t))\right)^2 \mathrm{d}\Omega \\ &+ \lambda_1 \int_\Omega \left(\|f_{,u}(\boldsymbol{x},t)\|_2^2 + \|f_{,v}(\boldsymbol{x},t)\|_2^2 + \|f_{,w}(\boldsymbol{x},t)\|_2^2 \right) \mathrm{d}\Omega \\ &+ \lambda_2 \int_\Omega \Big(\|f_{,u}(\boldsymbol{x},t)\|_2^2 \, \|f_{,v}(\boldsymbol{x},t)\|_2^2 - (< f_{,u}(\boldsymbol{x},t), f_{,v}(\boldsymbol{x},t) >)^2 \Big) \\ &+ \Big(\|f_{,v}(\boldsymbol{x},t)\|_2^2 \, \|f_{,w}(\boldsymbol{x},t)\|_2^2 - (< f_{,v}(\boldsymbol{x},t), f_{,w}(\boldsymbol{x},t) >)^2 \Big) \\ &+ \Big(\|f_{,u}(\boldsymbol{x},t)\|_2^2 \, \|f_{,w}(\boldsymbol{x},t)\|_2^2 - (< f_{,u}(\boldsymbol{x},t), f_{,w}(\boldsymbol{x},t) >)^2 \Big) \mathrm{d}\Omega, \end{aligned} \tag{26}$$

where the first term measures the sum of squared differences of the intensity between the iteratively updated source and target images, and λ_1 and λ_2 are regularization parameters that penalize non-smoothness and inconsistent area change of each face of the 3D control grid elements during deformation. The terms $f_{,u}(\boldsymbol{x},t), f_{,v}(\boldsymbol{x},t)$ and $f_{,w}(\boldsymbol{x},t)$ are the first derivatives of $f(\boldsymbol{x},t)$ with respect to coordinates $\{u, v, w\}$, and $g(\boldsymbol{x},t)$ is given by

$$g(\boldsymbol{x},t) = \frac{1}{\sqrt{\gamma + \left(\frac{\partial I_1(f(\boldsymbol{x},t))}{\partial u}\right)^2 + \left(\frac{\partial I_1(f(\boldsymbol{x},t))}{\partial v}\right)^2 + \left(\frac{\partial I_1(f(\boldsymbol{x},t))}{\partial w}\right)^2}}, \tag{27}$$

where γ is a small number to prevent division by zero. The gradient flow form for minimization of E is:

$$\frac{\mathrm{d}\boldsymbol{P}_m(t)}{\mathrm{d}t} = -\delta E_m(f(\boldsymbol{x},t)). \tag{28}$$

Control points are updated using the Forward Euler method and by introducing a pseudo timestep ϵ. The control points $P_m(t)$ are iteratively computed for time point $s+1$ based on the solution of the previous timestep s as follows

$$\boldsymbol{P}^{s+1} = \boldsymbol{P}^s - \epsilon\, \delta E^s(f(\boldsymbol{x},t)). \tag{29}$$

$\delta E^s(f(\boldsymbol{x},t))$ is the derivative of the energy functional with respect to parametric domain $\boldsymbol{x}$, see Ref. [30] for a detailed derivation. The optimization loop ends when the change in intensity difference falls below a given tolerance. We direct the reader to Ref. [30] for a detailed derivation of the registration framework. In the work presented here, we embed our images in an initial three-dimensional grid of size $32 \times 32 \times 32$ control points, set maximum number of refinement steps to 3, regularization parameters λ_1 and λ_2 to 0.0001 and 0.0001, respectively, and chose a timestep size of $1{\times}10^{-5}$.
We used the registration framework to determine the four deformation fields between weeks 21 and 22, weeks 22 and 23, weeks 23 and 24 and weeks 24 and 25. For each pair, we selected the first week as the source image and the second week as the target image. It took 22 iterations for the first two steps of 21-22 and 22-23 weeks, 24 iterations for 23-24 weeks and 57 iterations for 24-25 weeks to obtain the optimal transformation map with an average similarity ratio of 81.95%. This increase in iterations reflects the evolving morphological complexity of the progressive developmental steps. Local spline refinement increased the number of active degrees of freedom on average by a factor of 5.3; additional convergence properties are summarized in Table 3.

6 Growth-Induced Full-Field Brain Deformations

Following the registration step, we extracted the displacement vector of each control point in our grid. In Figure 4 we show the undeformed and deformed grids on a coronal and axial slice for all four

	week 21 to 22	week 22 to 23	week 23 to 24	week 24 to 25
max active DOF	179293	184738	211560	260623
# iterations	22	22	24	57
similarity ratio (RS) [%]	84.87	69.86	86.06	87.00

Table 3: Convergence properties of the registration framework. We achieve a mean similarity ratio of 81.95% after registering two consecutive weeks. Local spline refinement increased the number of active DOFs on average by a factor of 5.3.

registration steps. The effect of the regularization terms is clearly reflected in the smoothness of the deformation field throughout the brain. Simultaneously, the week-wise registration steps allow identification of the major folding event, i.e. the formation of the central sulcus, at week 24. Increased grid density leads to a higher spatial resolution of the three-dimensional deformation field and improves the detection of local growth phenomena.

Figure 5 shows registration results for changes between weeks 24 and 25 in three representative slices, the coronal, axial and sagittal views, respectively. The magnified images reveal the grid deformation and identify local growth patterns that produce highly heterogeneous deformation fields. Two challenges are encountered in the steps of MR image registration and computation of growth-induced deformation:

Newly formed brain regions limit the registration framework:
The registration framework faces significant challenges when new substructures emerge between two distinct scans. In general, the registration framework assumes that all material points are preserved and simply undergo a potentially large deformation. The generation of new material points leads to non-uniformities and incompatibilities in the displacement field which we have not yet addressed in the present work. Therefore, our approach provides reliable displacement data in the case of morphogenetic growth which manifests in the form of pure volumetric expansion. In this case, material points preserve their intensity value in MR images and simply displace. When new material emerges and influences the intensity distribution, the registration framework is observed to artificially distort the grid. Therefore, we are limited to one-week intervals over which the emergence of new substructures is minimal.

Heterogeneous Growth Field:
In order to prepare data for the inverse problem, we use the nodal displacement vectors in our FE meshes for weeks 21 through 24 to determine the reference configurations. Specifically, we use trilinear interpolation in the registration data to obtain the full-field displacement data for every node in each mesh based on the registration results from that particular week. Figure 6 shows the respective results as displacement vectors that are color-coded by magnitude. Earlier weeks (21 to 23) are characterized by rather homogeneous small displacements across the cortex. Later weeks (23 to 25) exhibit increasingly heterogeneous displacements which is characteristic for localization of growth due to the formation of the central sulcus, and the subsequent formation of folds within each lobe. The rapid proliferation and migration of neurons during this period of development [5] leads to an acceleration of brain growth. The observed growth patterns are also indicative that brain development is significantly more complex than purely uniform, morphological growth but must adhere to genetically encoded cell migration patterns that result in the highly reproducible brain topology observed within any species. The top row of Figure 6 shows the displacement field of the outer cortical surface; the bottom row shows the displacement field of the ventricular surface. We measured a maximum displacement of 5.79 mm in the temporal lobe between weeks 24 and 25. We observe mean displacements of the outer cortical surface of 0.45 ± 0.27 mm between weeks 21 and 22, 0.88 ± 0.42 mm between weeks 22 and 23, 1.91 ± 0.74 mm between weeks 23 and 24 and 3.03 ± 1.06 mm between weeks 24 and 25. Mean displacements of the ventricular surface are 0.19 ± 0.13 mm between weeks 21 and 22, 0.28 ± 0.19 mm between weeks 22 and 23, 0.8 ± 0.51 mm between weeks 23 and 24 and 1.49 ± 0.7 mm between weeks 24 and 25. Overall, we find that growth is highly symmetric during this early stage of brain development and posit that individual differences between hemispheres are the result of averaging data from multiple brains when the atlas was constructed [16].

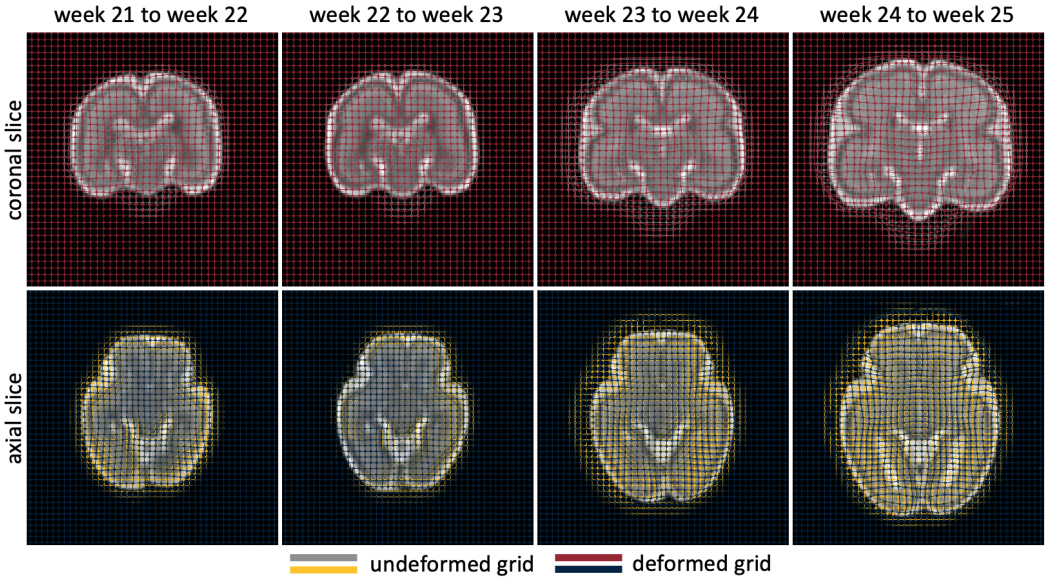

Figure 4: The registration framework iteratively updates the positions of control points that belong to the spline object embedded in each week's MRI data. Here, we plot the undeformed and deformed grids in representative coronal and axial slices for the registrations between weeks 21 and 22, weeks 22 and 23, weeks 23 and 24 and weeks 24 and 25. From the MRI images we observe the overall volume increase of the brain during the 5 week period. The two grids per image show the increasingly heterogeneous displacement field with rather uniform morphogenetic growth between weeks 21 and 23 and more localized displacement patterns in individual lobes between weeks 23 and 25.

6.1 Gaussian Filtering

While filtering techniques typically are applied to raw MRI data to generate the images in Figure 3a, noise is reintroduced by the registration algorithm. The displacement field reported in Figures 5-6 is therefore in need of smoothing before its use in the numerical techniques of inverse modelling. We applied Gaussian filtering to the post-registration displacement field, noting however, that the standard discrete Gaussian filter cannot be applied in a straightforward manner to unstructured meshes that must be used for the irregular geometry of the brain. Consider the continuous Gaussian filter over the infinite domain:

$$\begin{aligned}\widehat{\boldsymbol{u}}(\boldsymbol{x}_0) &= \int_{\mathbb{R}^3} G(\boldsymbol{x}_0,\boldsymbol{x})\boldsymbol{u}_{\text{reg}}(\boldsymbol{x})\mathrm{d}V \\ &= \int_{\Omega} G(\boldsymbol{x}_0,\boldsymbol{x})\boldsymbol{u}_{\text{reg}}(\boldsymbol{x})\mathrm{d}V,\end{aligned}$$

where $G(\boldsymbol{x}_0,\boldsymbol{x}) = \frac{1}{\left(\sqrt{2\pi\sigma^2}\right)^3} e^{-\frac{\|\boldsymbol{x}\|^2}{2\sigma^2}}$ is the three-dimensional Gaussian distribution, σ is the standard deviation and $\boldsymbol{u}_{\text{reg}}$ is the displacement field after registration. Since $\int_\Omega G\mathrm{d}V < 1$ we scale the filtered displacement at each node to obtain:

$$\begin{aligned}\widehat{\boldsymbol{u}}(\boldsymbol{x}_0) &= \frac{\int_{\mathbb{R}^3} G(\boldsymbol{x}_0,\boldsymbol{x})\mathrm{d}V}{\int_\Omega G(\boldsymbol{x}_0,\boldsymbol{x})\mathrm{d}V}\int_\Omega G(\boldsymbol{x}_0,\boldsymbol{x})\boldsymbol{u}_{\text{reg}}(\boldsymbol{x})\mathrm{d}V \\ &= \frac{1}{\int_\Omega G(\boldsymbol{x}_0,\boldsymbol{x})\mathrm{d}V}\int_\Omega G(\boldsymbol{x}_0,\boldsymbol{x})\boldsymbol{u}_{\text{reg}}(\boldsymbol{x})\mathrm{d}V. \qquad (30)\end{aligned}$$

7 Inference of the fetal brain's growth deformation tensor

The displacement field data for weeks τ to $\tau+1$ obtained after registration and filtering, as detailed in §4–6, is $\widehat{\boldsymbol{u}}_\tau$. The corresponding nodal values on various meshes are $\widehat{\boldsymbol{d}}_\tau$. As explained at the

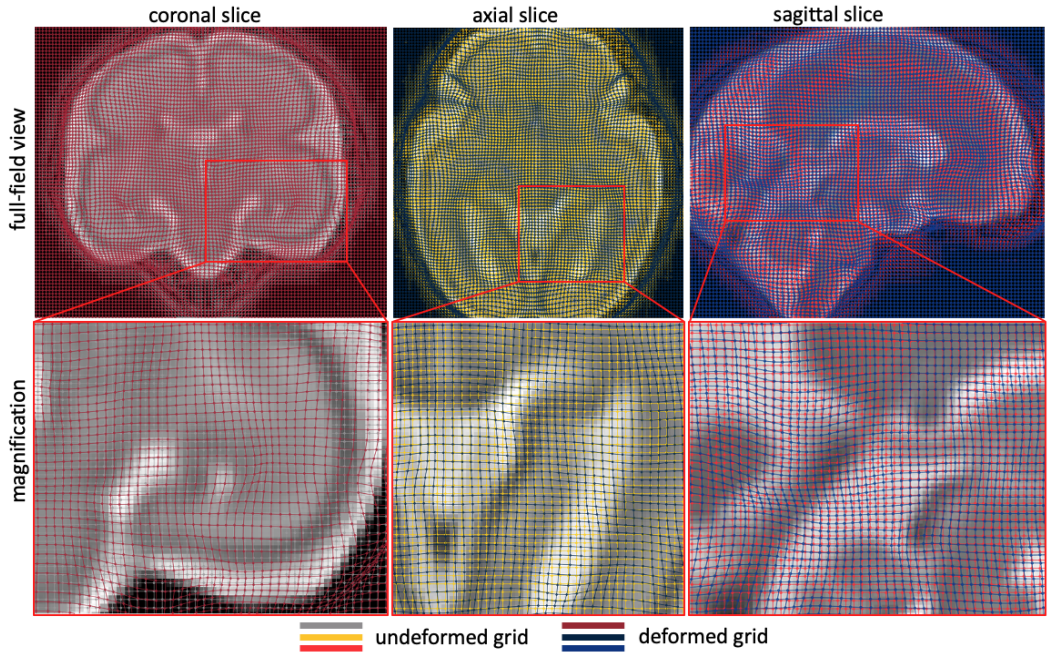

Figure 5: Coronal, axial and sagittal views of the registration results for week 24 to 25. We notice increasingly heterogeneous displacement patterns due to localized growth in distinct subregions of the brain. The registration framework delivers highly smooth displacements of the control points- to the extent that some local phenomena might be eliminated due to over-regularization of the spline object. As a consequence of this smoothing, the emergence of new substructure between two scans will lead to artificial grid distortions. Overall, the registration delivers a reliable displacement field representative of the temporally and spatially varying growth patterns [5].

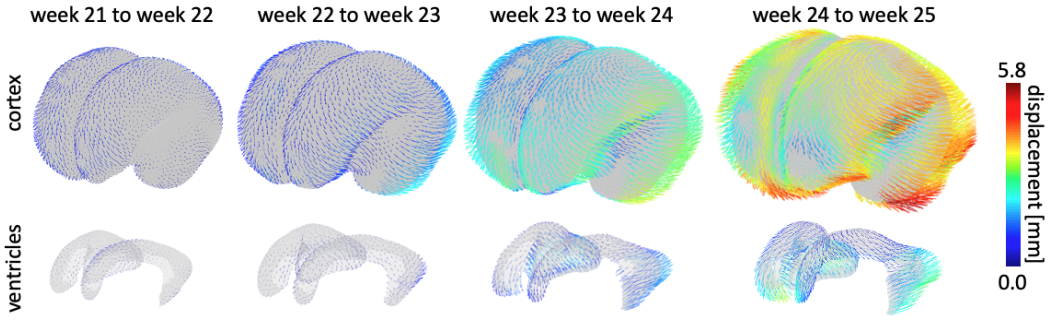

Figure 6: Full-field displacement data between week 21 and 22, week 22 and 23, week 23 and 24 and week 24 and 25. We observe a homogeneous displacement field between weeks 21 and 23 and increasingly heterogeneous displacement patterns between week 23 and 25. Specifically, we notice that the emergence of the central sulcus leads to localization of growth patterns that are attributed to the onset of secondary buckling in individual lobes and increased folding of the cortical surface. A maximum displacement of 1.24 mm was observed from week 21 to 22, 2.29 mm was observed from week 22 to 23, 3.65 mm was observed from week 23 to 24 and 5.79 mm from week 24 to 25.

end of §3.2, we used adjoint-based gradient optimization guided by the lower volume-averaged L^2-errors obtained relative to optimization by gradient descent. The following subsections discuss the meshes used, further interpolation of data between $\widehat{\boldsymbol{d}}_\tau$ and $\widehat{\boldsymbol{d}}_{\tau+1}$ to aid convergence, initialization of $\boldsymbol{\chi}$ (nodal values of $\boldsymbol{F}^{\mathrm{g}}$) and numerical performance. Results are presented as tables and figures for the volume-averaged L^2-errors, Equation (24) with $\widehat{\boldsymbol{u}} = \widehat{\boldsymbol{u}}_\tau$ and figures for the inferred fields of $\boldsymbol{F}^{\mathrm{g}}$.

7.1 Meshes

The MRI data at weeks 21 and 23 yield the corresponding reference configurations, Ω_{21} and Ω_{23}, on which tetrahedral meshes were constructed with 27306 and 32385 elements, respectively. Reference configurations Ω_{22} and Ω_{24} were then generated by deforming Ω_{21} and Ω_{23}, respectively, using the displacement fields $\widehat{\boldsymbol{u}}_{21}$ and $\widehat{\boldsymbol{u}}_{23}$ obtained by MRI registration for week 21-22 and week 23-24. These displacement fields applied to the meshes on Ω_{21} and Ω_{23} also yield the meshes on Ω_{22} and Ω_{24}. All these meshes appear in Figure 11.

7.2 Data interpolation to aid convergence

The displacement field data, $\widehat{\boldsymbol{u}}_{23}$, between weeks 23 and 24, results in large distortions that appear in the deformation gradient, $\widehat{\boldsymbol{F}}_{23}$. Since this field also drives, and confers these distortions on, the iterates of the inferred $\boldsymbol{F}^{\mathrm{g}}_{23}$, it makes the forward solution for $\boldsymbol{u}_{23}$ numerically stiff and prone to divergence in the adjoint-based gradient optimization. We therefore carried out a linear interpolation and redefined the displacement on Ω_{23} to be $\widetilde{\boldsymbol{u}}_{23} = \frac{1}{2}\widehat{\boldsymbol{u}}_{23}$ to an interpolated reference configuration $\Omega_{23.5}$. In a continuation of this interpolation, we also defined $\widetilde{\boldsymbol{u}}_{23.5} = \frac{1}{2}\widehat{\boldsymbol{u}}_{23}$ on $\Omega_{23.5}$ to Ω_{24}. In a further magnification of this large morphoelastic growth, $\widehat{\boldsymbol{u}}_{24}$ between weeks 24 and 25 leads to even greater distortions and more severe divergence of the forward solution for $\boldsymbol{u}_{24}$ during adjoint-based gradient optimization. We therefore defined eight intermediate displacement fields $\widetilde{\boldsymbol{u}}_{24}, \widetilde{\boldsymbol{u}}_{24.125}, \ldots \widetilde{\boldsymbol{u}}_{24.875} = \frac{1}{8}\widehat{\boldsymbol{u}}_{24}$ and the corresponding interpolated reference configurations $\Omega_{24.125}, \ldots \Omega_{24.875}$. These interpolated geometries represent the evolving reference configurations discussed in Section 2.1. Given these interpolated displacement fields, we aimed to infer the growth deformation tensor, $\boldsymbol{F}^{\mathrm{g}}_{\tau}$, between reference configurations Ω_{τ} and $\Omega_{\tau+\Delta\tau}$ defined as above.

The initial guess at each configuration $\boldsymbol{F}^{\mathrm{g}}_{\tau_0}$ was chosen to be diagonal and assembled from the corresponding components of the deformation gradient tensor $\widehat{\boldsymbol{F}}_{\tau} = \mathbf{1} + \partial\widehat{\boldsymbol{u}}_{\tau}/\partial\boldsymbol{X}_{\tau}$ or $\widetilde{\boldsymbol{F}}_{\tau} = \mathbf{1} + \partial\widetilde{\boldsymbol{u}}_{\tau}/\partial\boldsymbol{X}_{\tau}$ (if displacement interpolation to intermediate reference configurations was used). The nodal values, $\boldsymbol{\chi}_{\tau_0}$ were then obtained by solving the L^2-projection:

$$\begin{aligned}
&\int_{\Omega} \boldsymbol{\Xi} \colon \left(\boldsymbol{\chi}_{\tau_0} - \mathrm{diag}\left[\widehat{\boldsymbol{F}}_{\tau}\right]\right) \mathrm{d}V = 0 \text{ if } \widetilde{\boldsymbol{u}}_{\tau} \text{ has } \textit{not} \text{ been defined,} \\
&\int_{\Omega} \boldsymbol{\Xi} \colon \left(\boldsymbol{\chi}_{\tau_0} - \mathrm{diag}\left[\widetilde{\boldsymbol{F}}_{\tau}\right]\right) \mathrm{d}V = 0 \text{ if } \widetilde{\boldsymbol{u}}_{\tau} \text{ has been defined,}
\end{aligned} \tag{31}$$

with $\boldsymbol{\Xi}$ being the variations on $\boldsymbol{\chi}_{\tau_0}$.

7.3 Convergence

Our approach to the inverse problem involves iterations in which the adjoint equation is used to update $\boldsymbol{\chi}_{\tau}$, which is then interpolated for $\boldsymbol{F}^{\mathrm{g}}_{\tau}$. Each solution of the adjoint equation is followed by a forward solution for $\boldsymbol{u}_{\tau}$. In order to mollify numerical stiffness and ease the direct solver's path to convergence, we linearly subdivided $\boldsymbol{\chi}_{\tau}$ into 100 steps in driving the forward solution. The convergence threshold was set to requiring that the loss (see Equation 17) be smaller than 2×10^{-2} of $\|\widehat{u}_{\tau}\|_{\infty}$, and that the relative change in loss between successive adjoint solution steps falls below 10^{-3}.

7.4 Results

Gaussian filtering with zero means and standard deviations $\sigma = 0,\ 0.5$ mm were used on all the data, except for $\widehat{\boldsymbol{u}}_{24}$, which was also subjected to the $\sigma = 1$ mm filter. Table 4 includes results with $\sigma = 0,\ 0.5$ mm. Filtering leads to a lower volume-averaged L^2-error between the MRI data and the forward displacement solution driven by the inverted growth deformation gradient field for all cases. However, filtering reduces $\|\widehat{\boldsymbol{u}}_{\tau}\|_{\infty}$ to a degree, especially because surface effects truncate the integrals where the raw displacement is expected to be greatest.

Figure 7 shows the final forward displacement field solution, $\boldsymbol{u}_{\tau}$, obtained during the adjoint-based gradient optimization using data subjected to filtering with $\sigma = 0$. The top and bottom row

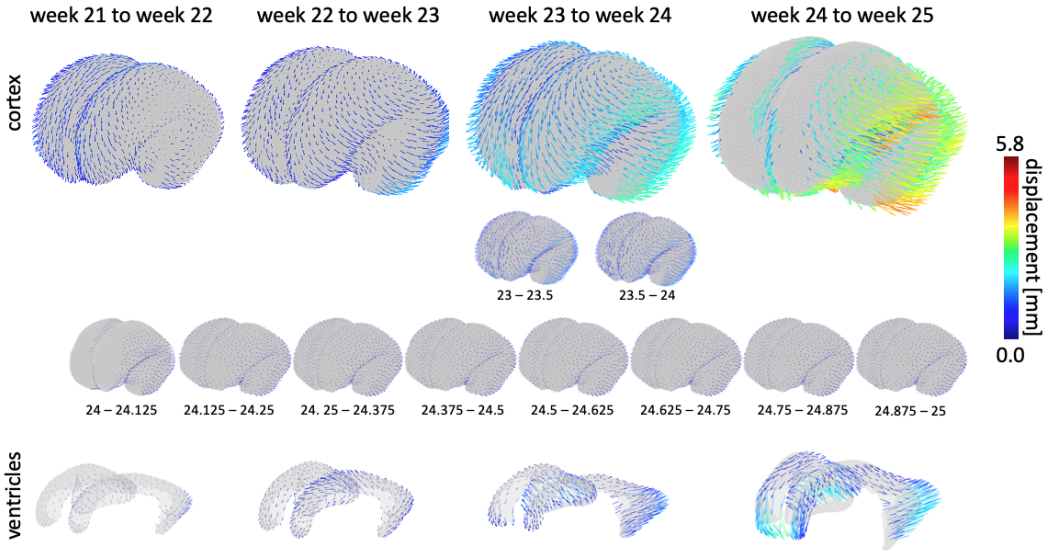

Figure 7: Inferred displacement fields between weeks 21-22, weeks 22-23, weeks 23-24 and weeks 24-25 using our adjoint-based optimization approach and shown here for the cortical and ventricular surface. Changes between weeks 23-24 and weeks 24-25 are broken into 2 and 8 substeps, respectively. Magnitude and orientation of the displacement vectors show remarkable agreement with the registration results shown in Figure 6.

in Figure 7, show the inferred displacement field $\boldsymbol{u}_\tau$ on the cortical and ventricular surfaces and are counterparts to Figure 6 which showed the displacement data fields after registration. This comparison provides a visual understanding of how close the inferred $\boldsymbol{F}^{\mathrm{g}}_\tau$ is to the unknown, true $\widehat{\boldsymbol{F}}^{\mathrm{g}}_\tau$, using the displacement fields as surrogates. The second and third row show the forward displacement fields corresponding to the interpolated $\widetilde{\boldsymbol{u}}_\tau$ fields. Note that in each case, these are *incremental* fields, for which reason, interpolation into more steps over 23-24 and 24-25 weeks results in smaller magnitudes $\boldsymbol{u}_\tau$. As a result, over 24-25 weeks, in particular, it appears that the forward displacement solution has lower magnitude than the MRI displacement data by registration. The corresponding error between the inferred displacement field and the MRI displacement data by registration is shown in Figure 8. Higher errors appear over the frontal, parietal and occipital lobes, and over the cerebellum, where the MRI displacement data have greater magnitudes. Table 4 shows, for each stage (by week or at interpolated instants) of the inference, the maximum displacement $\|\widehat{\boldsymbol{u}}\|_\infty$ and volume-averaged L^2-norm of the error, as defined in Equation (24). Note that $\|e(\boldsymbol{u})\|_2 \leq 2 \times 10^{-2}\|\widehat{\boldsymbol{u}}\|_\infty$ at each stage. Furthermore, on summing $\|e(\boldsymbol{u})\|$ over the eight steps interpolating between weeks 24 and 25 and using the triangle inequality, it follows that the total volume-averaged L^2-error in the forward displacement field from the inference relative to the MRI displacement data is bounded from above by 4.3×10^{-2}.

The main goal of this study is the inference of $\boldsymbol{F}^{\mathrm{g}}_\tau$ fields at the time instants, τ, from adjoint-based gradient optimization. Following inference and before plotting in the figures that follow, these fields were smoothed by Gaussian blurring (Equation 30 with $\sigma = 0.5$) in order to minimize artifacts introduced by mesh topology. Figure 9 shows the volume change induced by growth alone—i.e., discounting elastic deformation—via $\det\boldsymbol{F}^{\mathrm{g}}_\tau$ on three representative slices: the coronal, axial and sagittal planes, respectively. Recall that $\det\boldsymbol{F}^{\mathrm{g}}_\tau$ is the volume change induced at each stage τ by cell division, growth and migration. Figure 9 therefore offers, to our knowledge, the first data-driven inference of these cell dynamics that are the cause of morphoelastic brain growth, and ultimately of its folding. We draw attention to the radial distribution of growth, seen best in the axial, coronal and sagittal sections and increasing from lower values near the ventricles to higher in the cortex. This distribution is the first data-driven confirmation of the assumption underlying the morphoelastic theory of brain folding: that growth is radially distributed, increasing along the ventricular-cortical direction. Note that the interpolation of morphoelastic growth displacements over eight steps between 24 and 25 weeks, combined with the treatment using evolving reference configurations, renders the inferred

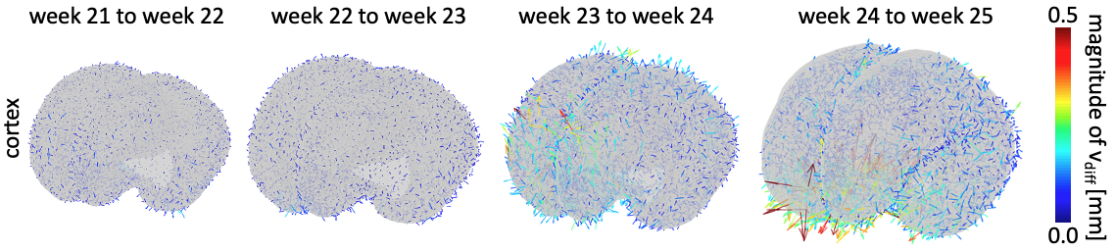

Figure 8: Error vectors representing the difference between the inferred displacement fields and registration-based displacement fields. Maximum absolute error is smaller than 0.5mm and is primarily observed in the frontal lobe for later weeks during which overall brain growth accelerates. Generally, we observe a homogeneous distribution of the magnitude and orientation across all weeks. *Arrow size is amplified by factor 20 for visualization purposes.*

$\det\boldsymbol{F}^{\mathrm{g}}_{24}, \dots \det\boldsymbol{F}^{\mathrm{g}}_{24.875}$ smaller than $\det\boldsymbol{F}^{\mathrm{g}}_{21}, \dots \det\boldsymbol{F}^{\mathrm{g}}_{23.5}$. However, the same pattern of radially distributed growth, increasing from ventricles to the cortical surface, is seen for the eight steps between 24 and 25 weeks when replotted over a narrower range in Figure 10. Also, the volume-averaged $\det\boldsymbol{F}^{\mathrm{g}}$ in the cortex is larger than in the subcortex in all cases, except for growth between 22 and 23 weeks (see Table 5). This strain mismatch between the layers is additional quantitative validation of the kinematic assumption commonly used in morphoelastic growth theories and that drives the emergence of folding, wrinkling and creasing.

While it is suggestive to gain a measure of the total growth over 24 to 25 weeks by multiplying $\det\boldsymbol{F}^{\mathrm{g}}_{24} \times \det\boldsymbol{F}^{\mathrm{g}}_{24.125} \cdots \times \det\boldsymbol{F}^{\mathrm{g}}_{24.875}$, this is not mathematically correct according to the treatment of evolving reference configurations. That is, there is no notion of a quantity, say $\overline{\boldsymbol{F}}^{\mathrm{g}}_{24-25} = \boldsymbol{F}^{\mathrm{g}}_{24.875}\boldsymbol{F}^{\mathrm{g}}_{24.75} \dots \boldsymbol{F}^{\mathrm{g}}_{24}$ representing pure growth kinematics between 24 and 25 weeks.

Through Figures 9 and 10 it also emerges that cell dynamics-induced growth is indeed localized in the frontal, parietal and occipital lobes, and the cerebellum.

Finally, the effect on the inferred $\boldsymbol{F}^{\mathrm{g}}_{\tau}$ fields from Gaussian filtering of the MRI displacement data (introduced at the beginning of this section) is presented in the Appendix as Figure 12. Larger filters smooth out the displacement fields obtained from MRI data, and also contribute to a more uniform distribution of $\det\boldsymbol{F}^{\mathrm{g}}_{\tau}$.

8 Conclusions

The morphoelastic theory of growth has formed the basis of a large body of computational work on brain development. However, to the best of our knowledge, it has not been used previously to make inferences on the nature of morphogenesis over the course of development. Our communication takes a step in this direction by building on fetal brain atlases. For it, we have gathered a diversity of methods: MR imaging, segmentation and registration to obtain raw data on the evolving displacement fields that can be regarded as the mapping underlying the geometric changes in the brain over many weeks of development, and inverse modelling to infer the growth tensor via optimization techniques. Notably, the registration techniques that yield displacement data themselves use inverse modelling and L^2 gradient flow-based optimization. The optimization methods that we explored for inferring the growth tensor included gradient descent of a physics-constrained loss function, and separately, adjoint-based gradient optimization, also with the same physics constraint—the satisfaction of the PDEs of morphoelastic growth in weak form. Also notable among our methods is the casting of morphoelastic growth in the framework of evolving reference configurations. Without this version of the morphoelastic growth theory, the problem would become numerically intractable due to the extremely large changes in morphology even over just weeks 21-25 of fetal development.

We note that the results of the inference consistently show that cell dynamics distributes growth radially, increasing from the ventricles to the cortical surface. While the central sulcus begins to form prominently over weeks 24-25, we anticipate that the persistence of this radial distribution leads to the multiscale folding, wrinkling and creasing, whose simulation has been the main goal of previous forward computations of brain morphogenesis—albeit without the strongly data-driven approach that

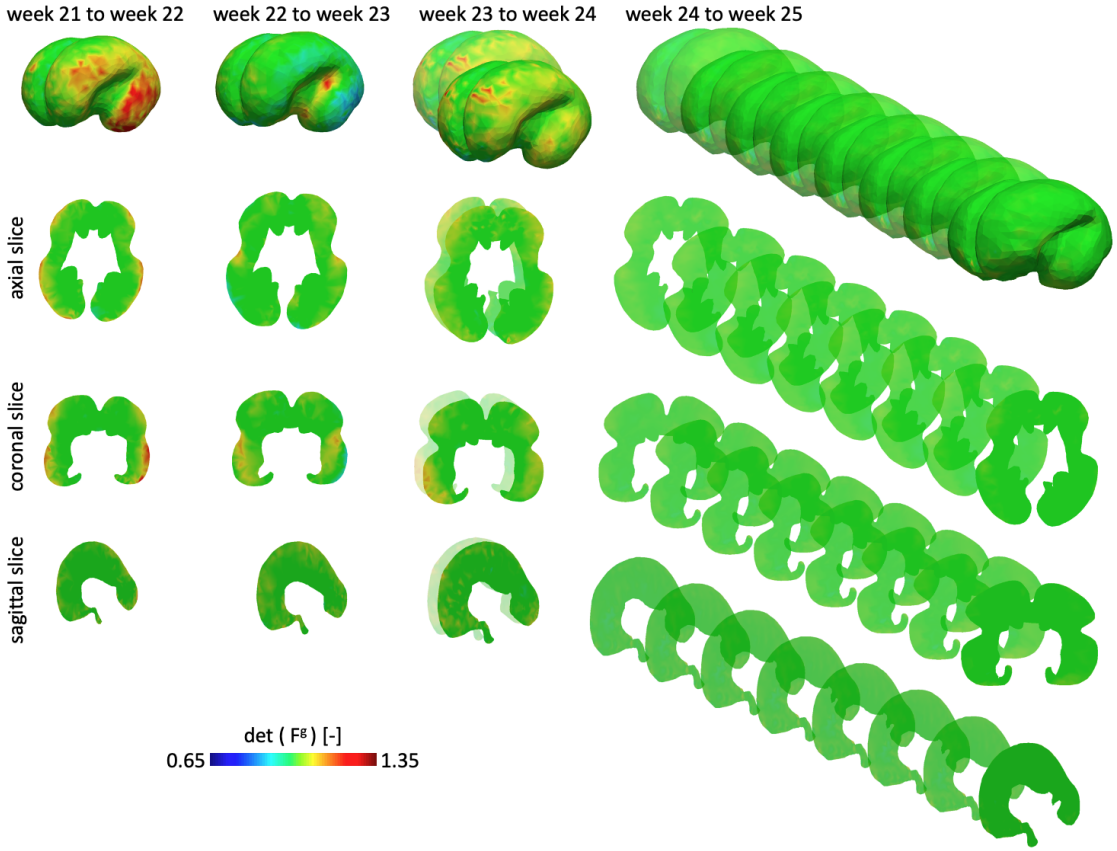

Figure 9: We calculate the determinant of the inferred growth deformation tensor $\det \boldsymbol{F}^{\mathrm{g}}$ for all weeks and show them here on the 3D geometry, as well as in representative axial, coronal and sagittal slices. The determinant ranges from 0.65 to 1.36 indicating both localized shrinking and expansion behavior. The growth fields differ between individual weeks suggesting a characteristic chronological order to brain development throughout gestation.

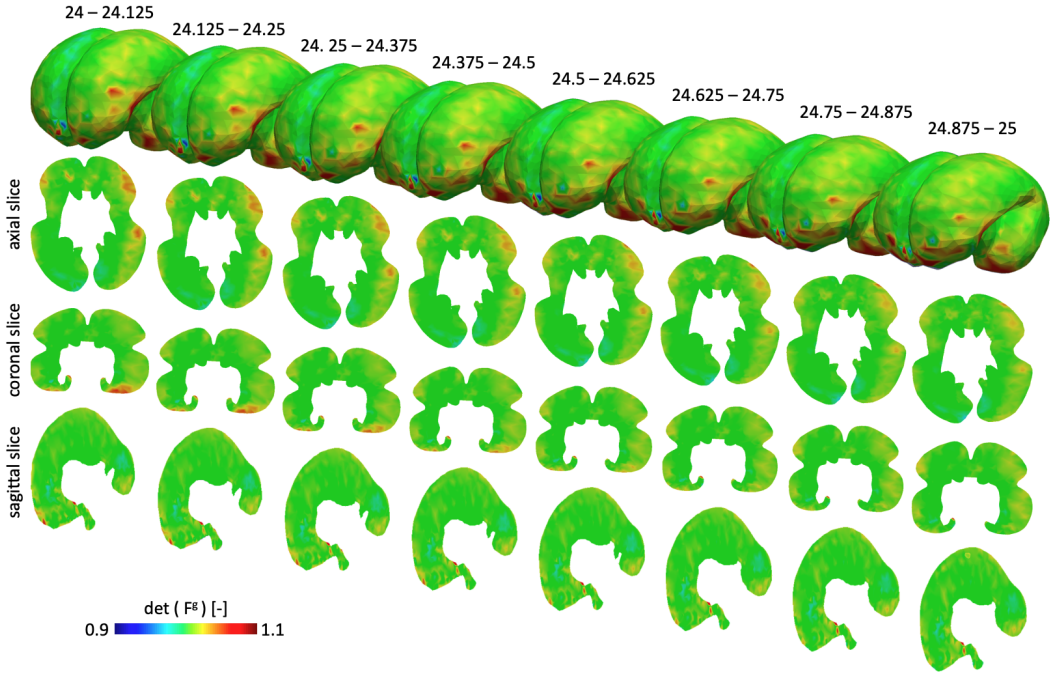

Figure 10: The determinant of the inferred growth deformation tensor $\det \boldsymbol{F}^{\mathrm{g}}$ at the eight intermediate steps between week 24 and 25 shown here with a re-scaled color range from 0.9 to 1.1. This closer look at changes between weeks 24 and 25 highlights the localized growth fields predominantly noticeable in the frontal and temporal lobes. The growth behavior is mostly symmetric with respect to both hemispheres.

we have adopted here.

The present work serves as a demonstration that the combination of brain atlas data and methods of image segmentation, registration and finally physics-constrained inverse modelling can provide greater insight to the developmental process.

Acknowledgements

This work was supported by the National Institute of Aging of the National Institute of Health under award R21AG067442 (Johannes Weickenmeier), and by the Defense Advanced Research Projects Agency (DARPA) under Agreement No. HR0011199002 (Krishna Garikipati and Zhenlin Wang).

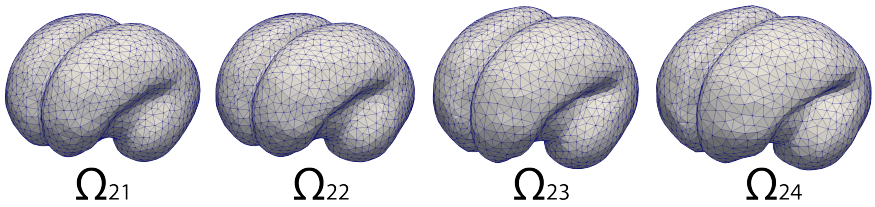

Figure 11: We generated tetrahedral meshes based on the segmentation at each gestational week 21 through 24 in support of our proposed theory of evolving reference configurations. At 24 weeks, the central sulcus begins to emerge and the temporal lobe expands noticeably.

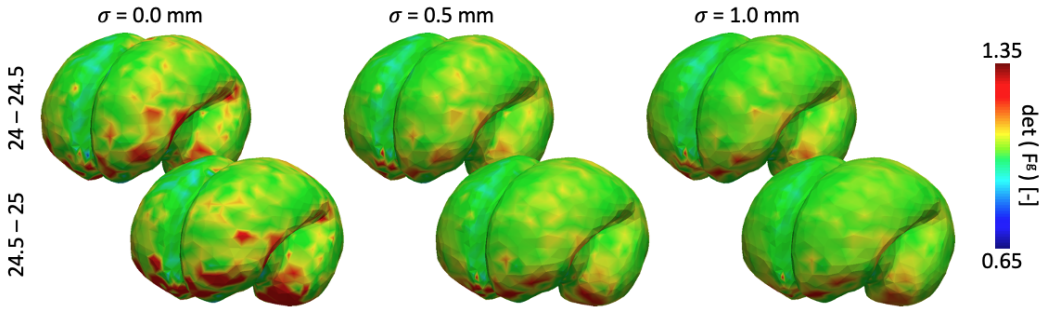

Figure 12: Gaussian filtering with increasing standard deviation σ leads to noticeable smoothing of the determinant of the inferred growth deformation tensor $\det \boldsymbol{F}^{\mathrm{g}}$, shown here for the example of changes between week 24 and 25 broken down into two steps.

Appendix

week	σ mm	$\|\widehat{\boldsymbol{u}}\|_\infty$ mm	$\|e(\boldsymbol{u})\|_2$ mm
21-22	0	1.8201×10^{0}	1.5233×10^{-2}
	0.5	1.5932×10^{0}	1.1700×10^{-2}
22-23	0	1.4246×10^{0}	1.4532×10^{-2}
	0.5	1.3070×10^{0}	1.1615×10^{-2}
23-23.5	0	1.4507×10^{0}	2.0958×10^{-2}
	0.5	1.2572×10^{0}	1.7730×10^{-2}
23.5-24	0	1.4507×10^{0}	2.1542×10^{-2}
	0.5	1.2572×10^{0}	1.7702×10^{-2}
24-24.125	0	4.0326×10^{-1}	6.7394×10^{-3}
	0.5	3.5334×10^{-1}	5.3730×10^{-3}
24.125-24.25	0	4.0326×10^{-1}	6.8180×10^{-3}
	0.5	3.5334×10^{-1}	5.4294×10^{-3}
24.25-24.375	0	4.0326×10^{-1}	6.6352×10^{-3}
	0.5	3.5334×10^{-1}	5.5020×10^{-3}
24.375-24.5	0	4.0326×10^{-1}	6.7756×10^{-3}
	0.5	3.5334×10^{-1}	5.3364×10^{-3}
24.5-24.625	0	4.0326×10^{-1}	6.9141×10^{-3}
	0.5	3.5334×10^{-1}	5.3310×10^{-3}
24.625-24.75	0	4.0326×10^{-1}	6.4876×10^{-3}
	0.5	3.5334×10^{-1}	5.3485×10^{-3}
24.75-24.875	0	4.0326×10^{-1}	6.3955×10^{-3}
	0.5	3.5334×10^{-1}	5.1621×10^{-3}
24.875-25	0	4.0326×10^{-1}	6.2983×10^{-3}
	0.5	3.5334×10^{-1}	5.0780×10^{-3}

Table 4: Results summary. The values of standard deviation σ correspond to Gaussian filtering of the registration data. From the triangle inequality, the total volume-averaged L^2-error in the forward displacement field from the inference relative to the MRI displacement data is bounded from above by 4.3×10^{-2} for either value of σ.

week	σ mm	Cortex		Sub-cortex	
		$\overline{\det \boldsymbol{F}^{\mathrm{g}}_{\tau}}$	$\max \det \boldsymbol{F}^{\mathrm{g}}_{\tau}$	$\overline{\det \boldsymbol{F}^{\mathrm{g}}_{\tau}}$	$\max \det \boldsymbol{F}^{\mathrm{g}}_{\tau}$
21-22	0	1.080	1.419	1.042	1.459
	0.5	1.058	1.239	1.036	1.371
22-23	0	1.031	1.413	1.041	1.398
	0.5	1.033	1.240	1.035	1.279
23-23.5	0	1.071	1.321	1.048	1.337
	0.5	1.057	1.346	1.044	1.252
23.5-24	0	1.071	1.367	1.048	1.364
	0.5	1.057	1.379	1.044	1.244
24-24.125	0	1.021	1.190	1.013	1.140
	0.5	1.016	1.146	1.012	1.089
24.125-24.25	0	1.021	1.211	1.013	1.152
	0.5	1.016	1.165	1.012	1.096
24.25-24.375	0	1.021	1.227	1.013	1.153
	0.5	1.016	1.176	1.012	1.095
24.375-24.5	0	1.021	1.229	1.013	1.136
	0.5	1.016	1.180	1.012	1.103
24.5-24.625	0	1.021	1.236	1.013	1.337
	0.5	1.0160	1.184	1.012	1.135
24.625-24.75	0	1.021	1.233	1.013	1.162
	0.5	1.016	1.185	1.012	1.166
24.75-24.875	0	1.021	1.226	1.013	1.178
	0.5	1.016	1.183	1.012	1.177
24.875-25	0	1.021	1.205	1.013	1.207
	0.5	1.016	1.184	1.012	1.194

Table 5: The volume-averaged $\det \boldsymbol{F}^{\mathrm{g}}_{\tau}$, denoted as $\overline{\det \boldsymbol{F}^{\mathrm{g}}_{\tau}}$ in the cortex is larger than in the sub-cortex in all cases except for weeks 22-23.

References

[1] Martin S. Alnæs, Jan Blechta, Johan Hake, August Johansson, Benjamin Kehlet, Anders Logg, Chris Richardson, Johannes Ring, Marie E. Rognes, and Garth N. Wells. "The FEniCS Project Version 1.5". In: *Archive of Numerical Software* 3.100 (2015). DOI: 10.11588/ans.2015.100.20553.

[2] D. Ambrosi, G.A. Ateshian, E.M. Arruda, S.C. Cowin, J. Dumais, A. Goriely, G.A. Holzapfel, J.D. Humphrey, R. Kemkemer, E. Kuhl, J.E. Olberding, L.A. Taber, and K. Garikipati. "Perspectives on biological growth and remodeling". In: *J. Mech. Phys. Solids* 59 (2011), pp. 863–883.

[3] P.V. Bayly, R.J. Okamoto, G. Xu, Y. Shi, and L.A. Taber. "A cortical folding model incorporating stress-dependent growth explains gyral wavelengths and stress patterns in the developing brain". In: *Phys. Biol.* 10 (2013).

[4] S. Budday, S. Andres, B. Walter, P. Steinmann, and E. Kuhl. "Wrinkling instabilities in soft bilayered systems". In: *Philosphical Transactions A* 375 (2017).

[5] S. Budday and P. Steinmann III E. Kuhl. "Physical biology of human brain development". In: *Front. Cell. Neurosci.* 9 (2015), p. 257.

[6] S. Budday, C. Raybaud, and E. Kuhl. "A mechanical model predicts morphological abnormalities in the developing human brain". In: *Scientific Reports* 4.5644 (2014), doi: 10.1038/srep05644.

[7] S. Budday, G Sommer, C. Birkl, C. Langkammer, J. Haybaeck, J. Kohnert, Paulsen Bauer M., Steinmann P. F., E. Kuhl, and G.A. Holzapfel. "Mechanical characterization of human brain tissue". In: *Acta Biomaterialia* 48 (2017), pp. 319–340.

[8] S. Budday, P. Steinmann, A. Goriely, and E. Kuhl. "Size and curvature regulate pattern selection in the mammalian brain". In: *Extreme Mechanics Letters* 4 (2015), pp. 193–198.

[9] S. Budday, P. Steinmann, and E. Kuhl. "Physical biology of human brain development". In: *Frontiers in Cellular Neuroscience* 9.257 (2015).

[10] S. Chatelin, A. Constantinesco, and R. Willinger. "Fifty years of brain tissue mechanical testing: From in vitro to in vivo investigations". In: *Biorheology* 47.5-6 (2010), pp. 255–276.

[11] J.A.W van Dommelen, T.P.J van der Sande, M. Hrapko, and G.W.M. Peters. "Mechanical properties of brain tissue by indentation: Interregional variation". In: *Journal of the Mechanical Behavior of Biomedical Materials* 3 (2 2010), pp. 158–166.

[12] D. C. van Essen. "A tension-based theory of morphogenesis and compact wiring in the central nervous system". In: *Nature* 385 (1997), pp. 313–318.

[13] K. Garikipati. "The kinematics of biological growth". In: *App. Mech. Rev.* 62 (2009).

[14] K. Garikipati, E. M. Arruda, K. Grosh, H. Narayanan, and S. Calve. "A continuum treatment of growth in biological tissue: The coupling of mass transport and mechanics". In: *J. Mech. Phys. Solids* 52 (2004), pp. 1595–1625.

[15] A. Gholipour, C. Limperopoulos, Clancy S., A. Clouchoux C.and Akhondi-Asl, J.A. Estroff, and S.K. Warfield. "Construction of a deformable spatiotemporal MRI atlas of the fetal brain: Evaluation of similarity metrics and deformation models". In: *MICCAI* (2014).

[16] A. Gholipour, C. K. Rollins, C. Velasco-Annis, A. Ouaalam, A. Akhondi-Asl, O. Afacan, C. M. Ortinau, S. Clancy, C. Limperopoulos, E. Yang, and J. A. Estroff. "A normative spatiotemporal MRI atlas of the fetal brain for automatic segmentation and analysis of early brain growth". In: *Sci. Rep.* 7.1 (2017), pp. 1–13.

[17] A. Gholipour, C.K. Rollins, C. Velasco-Annis, A. Ouaalam, O.and Ortinau C.M.and Clancy S.and Limperopoulous C.and Yang E.and Estroff J.A. Akhondi-Asl A.and Afacan, and S.K. Warfield. "A normative spatiotemporal MRI atlas of the fetal brain for automatic segmentation and analysis of early brain growth". In: *Scientific Reports* 7.476 (2017).

[18] A. Goriely. *The Mathematics and Mechanics of Biological Growth*. Springer, 2017.

[19] A. Goriely, M.G.D. Geers, G. A. Holzapfel, J. Jayamohan, A. Jerusalem, S. Sivaloganathan, W. Squier, J. A. van Dommelen, S. Waters, and E. Kuhl. "Mechancis of the brain: perspectives, challenges, and opportunities". In: *Biomech. Model. Mechanobiol.* 14 (2015).

[20] P. A. Habas, J. A. Scott, A. Roosta, V. Rajagopalan, Kio K. Kim, F. Rousseau, A. J. Barkovich, O. A. Glenn, and C. Studholme. "Early folding patterns and asymmetries of the normal human brain detected from in utero MRI". In: *Cereb. Cortex.* 22.1 (2012), pp. 13–25.

[21] P.A. Habas, J.A. Scott, A. Roosta, V. Rajagopalan, K. Kim, A. J. Barkovich, O. A. Glenn, and C. Studholme. "Early folding patterns and asymmetries of the normal human brain detected from in utero MRI". In: *Cerebral Cortex* 22 (2012), pp. 13–25.

[22] R. Hill and J. W. Hutchinson. "Bifurcation phenomena in the plane tension test". In: *J. Mech. Phys. Solids* 23 (1975), pp. 239–264.

[23] Barkovich A. J. "Current concepts of polymicrogyria". In: *Neuroradiology* 52 (2010), pp. 479–487.

[24] M. Kato and W.B. Dobyns. "X-linked lissencephaly with abnormal genitalia as a tangential migration disorder causing intractable epilepsy: Proposal for a new term, "Interneuronopathy"". In: *J. Child Neuro.* 20 (2005), pp. 392–397.

[25] Diederik P. Kingma and Jimmy Ba. *Adam: A Method for Stochastic Optimization.* 2014. arXiv: 1412.6980 [cs.LG].

[26] Sebastian K. Mitusch, Simon W. Funke, and Jørgen S. Dokken. "dolfin-adjoint 2018.1: automated adjoints for FEniCS and Firedrake". In: *Journal of Open Source Software* 4.38 (2019), p. 1292. DOI: 10.21105/joss.01292. URL: https://doi.org/10.21105/joss.01292.

[27] H. Narayanan, E. M. Arruda, K. Grosh, and K. Garikipati. "The micromechanics of fluid-solid interactions during growth in porous soft biological tissue". In: *Biomech. Model. Mechanobiol.* 8 (20009), pp. 163–181.

[28] P. P. Landrieu, B. Husson, D. Pariente, and C. Lacroix. "MRI-neuropathological correlations in type 1 lissencephaly". In: *Paediatric Neuroradiology* 40 (1998), pp. 173–176.

[29] T. Paus, F. Tomaiuolo, N. Otaky, D. MacDonald, M. Petrides, J. Atlas, and A. Morris R.and Evans. "Human cingulate and paracingulate sulci: pattern, variability, asymmetry, and probabilistic map". In: *Cerebral Cortex* 6 (1996), pp. 207–214.

[30] A. Pawar, Y. J. Zhang, C. Anitescu, Y. Jia, and T. Rabczuk. "DTHB3D_Reg: Dynamic Truncated Hierarchical B-Spline Based 3D Nonrigid Image Registration". In: *Commun. Comput. Phys.* 23.3 (2018).

[31] M.T. Prange and S.S. Margulies. "Regional, directional, and age-dependent properties of the brain undergoing large deformation". In: *Transactions of the ASME* 124 (2002), pp. 244–252.

[32] Rijk de Rooij and Ellen Kuhl. "A physical multifield model predicts the development of volume and structure in the human brain". In: *Journal of the Mechanics and Physics of Solids* 112 (2018), pp. 563–576.

[33] C. Seshardri, T. Devlina, A. Rudra, and S. Sujit. "Pachygyria presented as mania". In: *Indian Journal of Psychological Medicine* 37.4 (2016).

[34] T. Tallinen, J.S. Biggins, and L. Mahadevan. "Surface sulci in squeezed soft solids". In: *Phys. Rev. Lett.* 110 (2013).

[35] T. Tallinen, J. Chung, F. Rausseau, N. Girard, J. Lefevre, and L. Mahadevan. "On the growth and form of cortical convolutions". In: *Nature Phys.* 12 (2016), pp. 588–593.

[36] S.N. Verner and K. Garikipati. "A computational study of the mechanisms growth-driven folding patterns on shells, with application to the developing brain". In: *Extreme Mech. Lett.* 18 (2018), pp. 58–69.

[37] Pauli Virtanen, Ralf Gommers, Travis E. Oliphant, Matt Haberland, Tyler Reddy, David Cournapeau, Evgeni Burovski, Pearu Peterson, Warren Weckesser, Jonathan Bright, Stéfan J. van der Walt, Matthew Brett, Joshua Wilson, K. Jarrod Millman, Nikolay Mayorov, Andrew R. J. Nelson, Eric Jones, Robert Kern, Eric Larson, CJ Carey, İlhan Polat, Yu Feng, Eric W. Moore, Jake Vand erPlas, Denis Laxalde, Josef Perktold, Robert Cimrman, Ian Henriksen, E. A. Quintero, Charles R Harris, Anne M. Archibald, Antônio H. Ribeiro, Fabian Pedregosa, Paul van Mulbregt, and SciPy 1. 0 Contributors. "SciPy 1.0: Fundamental Algorithms for Scientific Computing in Python". In: *Nature Methods* 17 (2020), pp. 261–272. DOI: `https://doi.org/10.1038/s41592-019-0686-2`.

[38] J.J. Volpe, T.E. Inder, B.T. Darras, L.S. de Vries, and A.J. du Plessis. *Volpe's neurology of the newborn*. Elsevier, 2017.

[39] J Weickenmeier, CAM Butler, PG Young, Alain Goriely, and E Kuhl. "The mechanics of decompressive craniectomy: Personalized simulations". In: *Computer Methods in Applied Mechanics and Engineering* 314 (2017), pp. 180–195.

[40] J Weickenmeier, R de Rooij, S Budday, P Steinmann, TC Ovaert, and E Kuhl. "Brain stiffness increases with myelin content". In: *Acta Biomater* 42 (2016), pp. 265–272.

[41] G. Xu, A.K. Knutsen, K. Dikranian, C.D. Kroenke, P.V. Bayly, and L.A. Taber. "Axons pull on the brain, but tension does not drive cortical folding". In: *J. Biomed. Eng.* 132 (2010).

[42] J. Yin, Z. Cao, C. Li, I. Sheinman, and X. Chen. "Stress-driven buckling patterns in spheroidal core/shell structures". In: *PNAS* 105.49 (2008), pp. 19132–19135.

[43] W. Z. Huang Hong and Z. Suo. "Evolution of wrinkles in hard films on soft substrates". In: *Physical Review E* 70 (2004), p. 030601.

[44] K. Zilles, E. Armstrong, A. Schleicher, and H. Kretschmann. "The human pattern of gyrification in the cerebral cortex". In: *Anatomy and Embryology* 179 (1988), pp. 173–179.